

DnaJC7 binds natively folded structural elements in tau to inhibit amyloid formation

Lukasz Joachimiak (✉ lukasz.joachimiak@utsouthwestern.edu)

The University of Texas Southwestern Medical Center <https://orcid.org/0000-0003-3061-5850>

Zhiqiang Hou

UTSW medical center <https://orcid.org/0000-0001-8185-9025>

Pawel Wydorski

The University of Texas Southwestern Medical Center

Valerie Perez

The University of Texas Southwestern Medical Center <https://orcid.org/0000-0001-8854-515X>

Ayde Mendoza-Oliva

The University of Texas Southwestern Medical Center

Bryan Ryder

The University of Texas Southwestern Medical Center <https://orcid.org/0000-0003-1393-0875>

Hilda Mirbaha

The University of Texas Southwestern Medical Center

Omar Kashmer

The University of Texas Southwestern Medical Center

Article

Keywords: Molecular Chaperones, Binding Substrates, Tau Aggregation Regulation, Tau Conversion

Posted Date: January 4th, 2021

DOI: <https://doi.org/10.21203/rs.3.rs-129204/v1>

License:  This work is licensed under a Creative Commons Attribution 4.0 International License.

[Read Full License](#)

Version of Record: A version of this preprint was published at Nature Communications on September 9th, 2021. See the published version at <https://doi.org/10.1038/s41467-021-25635-y>.

1
2
3
4
5
6
7
8
9
10
11
12
13
14
15
16
17
18

DnaJC7 binds natively folded structural elements in tau to inhibit amyloid formation

Zhiqiang Hou^{1,2}, Pawel M. Wydorski¹, Valerie A. Perez^{1,3}, Aydé Mendoza-Oliva¹, Bryan D. Ryder^{1,3}, Hilda Mirbaha¹, Omar Kashmer¹, Lukasz A. Joachimiak^{1,4*}

¹ Center for Alzheimer’s and Neurodegenerative Diseases, University of Texas Southwestern Medical Center, Dallas, TX 75235, United States

² Department of Biophysics, University of Texas Southwestern Medical Center, Dallas, TX 75235, United States

³ Molecular Biophysics Program, University of Texas Southwestern Medical Center, Dallas, TX 75235, United States

⁴ Department of Biochemistry, University of Texas Southwestern Medical Center, Dallas, TX 75235, United States

* To whom correspondence should be addressed: Lukasz.Joachimiak@UTSouthwestern.edu

19 **ABSTRACT**

20

21 Molecular chaperones, including Hsp70/Hsp40 families, play central roles in binding substrates to prevent
22 their aggregation. How Hsp40s select different conformations of substrates remains poorly understood.
23 Here, we report a novel interaction between the Hsp40 DnaJC7 and tau that efficiently suppresses tau
24 aggregation *in vitro* and in cells. DnaJC7 binds preferentially to natively folded wild-type tau, but disease-
25 associated mutants in tau reduce chaperone binding affinity. We identify that DnaJC7 uses a single TPR
26 domain to recognize a β -turn element in tau that contains the ²⁷⁵VQIINK²⁸⁰ amyloid motif. Wild-type tau
27 β -turn fragments, but not mutant fragments, can block full-length tau binding to DnaJC7. These data
28 suggest DnaJC7 preferentially binds and stabilizes natively folded conformations of tau to prevent tau
29 conversion into amyloids. This identifies a novel mechanism of tau aggregation regulation that can be
30 exploited as both a diagnostic and a therapeutic intervention.

31

32 INTRODUCTION

33
34 Molecular chaperones maintain cellular homeostasis by reducing aggregation, preventing misfolding, and
35 stabilizing natively folded conformations. One of the most ubiquitous and conserved chaperone systems
36 is encoded by the 70kDa and 40kDa heat shock proteins (Hsp70s/Hsp40s), which participate in diverse
37 cellular functions that span protein folding, refolding, and degradation [1]. Hsp70/Hsp40 function is linked
38 to regulation of pathogenic protein conformations of tau, α -synuclein and others that cause
39 neurodegenerative diseases [2-7]. The Hsp70s clearly have an impact on misfolding diseases, but they
40 also play central roles in folding a large portion of the proteome and their dysregulation may have broader
41 impacts [8]. While the Hsp70 protein family is conserved, substrate specificity and selectivity are imparted
42 by Hsp40 co-chaperones. Hsp40s are thought to capture substrates and transfer them to an Hsp70 for
43 subsequent refolding [9]. Coordination of Hsp70 and Hsp40 activities enable high selectivity under
44 diverse cellular functions and broad sequence diversity of substrate proteins, but it is now recognized
45 that Hsp40s themselves encode capacity to effectively suppress protein aggregation [10, 11].

46
47 The human genome encodes 47 Hsp40s, of which a majority are expressed in the brain [12]. All the
48 members of the family contain a conserved J-domain (JD), which binds and activates Hsp70 for substrate
49 transfer. Hsp40s are classified into A, B, and C sub-families according to their domain organization. Class
50 A and B Hsp40s are considered general chaperones that bind to nascent, unfolded, or misfolded
51 aggregation-prone substrates and transfer them to Hsp70s [13, 14]. Little is known about the capacity of
52 Class C Hsp40 family members in substrate binding and folding due to their broad diversity of domain
53 organization and likely functions [15]. One such member of the C class Hsp40 family, DnaJC7 (TPR2;
54 Tetratricopeptide Repeat 2 protein) is highly expressed in the brain [16] and loss of DnaJC7 function is
55 implicated in amyotrophic lateral sclerosis (ALS) and other neurodegenerative diseases [17]. DnaJC7,
56 together with Hsp90 and Hsp70, has been implicated in the maturation of the glucocorticoid and
57 progesterone receptors [18, 19]. Further, DnaJC7 also plays a role in retaining the constitutive
58 active/androstane receptor (CAR) transcription factor in the cytosol and thus regulating gene activation
59 by CAR [20]. DnaJC7 is distinct among the Hsp40s in that it contains three tetratricopeptide repeat (TPR)
60 domains termed TPR1, TPR2a, and TPR2b. Chaperones that contain TPRs comprise approximately one

61 third of chaperone proteins, but the role of TPRs in substrate binding remain unknown [21]. Another
62 example of a TPR-containing chaperone is Hsp70-Hsp90 organizing protein (HOP), known as stress
63 inducible protein (STI1) in yeast, is composed of multiple TPRs which bind to Hsp70, Hsp90, and
64 substrate simultaneously to facilitate substrate transfer between Hsp70 and Hsp90 [22]. In addition to
65 TPR domains, DnaJC7 also encodes a J-domain suggesting that if it binds substrates, it may be able to
66 transfer them to Hsp70 like the canonical Hsp40s. Indeed, DnaJC7 has been associated with insoluble
67 Huntingtin polyglutamine aggregates, steroid receptor folding with Hsp90 and cytosolic retention of
68 CAR [20, 23, 24].

69
70 Here we report that DnaJC7 directly influences the aggregation properties of the microtubule associated
71 protein tau. Tau is an intrinsically disordered protein that plays important roles in stabilizing microtubules
72 [25]. In its native non-disease conformation tau is very stable and does not readily aggregate [26]. Recent
73 data suggest that the native conformation of tau monomer can convert into a pathogenic monomer seed
74 that initiates the disease process to amyloid fibril formation linked to many neurodegenerative diseases
75 [28]. We find that DnaJC7 preferentially associates with native conformations of tau isolated from
76 tauopathy mouse brains and CRISPR/Cas9 knockout of DnaJC7 promotes tau aggregation in cells. We
77 reconstituted the DnaJC7-tau interaction *in vitro* and used a combination of crosslinking-mass
78 spectrometry (XL-MS) and NMR to identify the binding surfaces between DnaJC7 and tau. DnaJC7 uses
79 the TPR2b domain to interact with a sequence element in the repeat domain of tau located between
80 repeats 1 and 2, termed R1R2. We show dramatic differences in affinity between WT tau and a
81 aggregation-prone disease-associated P301L tau mutant that can be explained by changes in the tau
82 dynamics, suggesting that DnaJC7 preferentially binds to the natively folded conformations of wild-type
83 tau. *In vitro* and in cells, DnaJC7 binding to tau efficiently suppresses seeded tau aggregation. While
84 each TPR domain individually can bind tightly to tau, the intact DnaJC7 chaperone is essential for
85 aggregation suppression activity *in vitro*. We employ XL-MS guided modelling to show how DnaJC7 binds
86 to R1R2 in a natively folded conformation consistent with NMR chemical shifts. Finally, we show that an
87 isolated natively folded R1R2 minimal fragment-derived from tau can block DnaJC7 binding to tau while
88 an R1R2 peptide encoding disease-associated proline to serine mutation cannot. Overall, our findings

89 indicate that DnaJC7 binds to natively folded tau, is an important modulator of tau aggregation *in vitro*
90 and in cells and may play a role in preventing the formation of pathogenic seeds in disease.

91

92 **Results**

93 **DnaJC7 influences tau seeding *in vivo* and in cells.**

94 We have recently shown that tau seeding species appear in a tauopathy mouse model (PS19) prior to
95 the appearance of tau pathology in the brain [28]. We sought to identify proteins that are bound to small
96 soluble tau species in this early window when the first soluble seeding species appear to gain insight into
97 novel cellular factors that could play a role in influencing tau aggregation. Soluble tau was
98 immunoprecipitated (IP) from young PS19 mouse brains aged from one week to six weeks and small
99 species isolated using Size Exclusion Chromatography (SEC) [28]. Each sample was assayed for
100 seeding capacity determined by transducing samples into tau biosensors cells expressing tau repeat
101 domain (herein tauRD) fused to CFP and YFP [29] and the extent of seeding was quantified by measuring
102 the FRET signal between the fluorescent fusion constructs, which reports on their intracellular assembly
103 into amyloids (Fig. 1a). In parallel, we employed mass spectrometry to identify co-factors bound to the
104 immunoprecipitated tau. We identified many known tau interactors including Hsp70s, 14-3-3, prolyl-
105 isomerases, Hsp90, and a series of Hsp40s (Supplementary Data 1). Overall, we discovered 9 Hsp40s
106 that co-purified with tau across each tau IP (Supplementary Data 1). Amongst them, we identified Hsp40s,
107 including DnaJA2, DnaJB1 and DnaJB6, which have been previously implicated in binding amyloidogenic
108 substrates to control fibril assembly or disassembly [30-32]. We find that tau signal intensity increased
109 10-fold across this time window and most chaperones trend with tau signal with some notable exceptions,
110 signal intensity for DnaJC7 decreased 5-fold while for DnaJC5 it increased nearly 50-fold (Supplementary
111 Fig. 1a). To understand the abundance of the different Hsp40s bound as a function of tau changes we
112 normalized the Hsp40 signal intensity according to the 1N4R tau intensities (see methods). Recently,
113 Hsp40s have been implicated in directly modulating protein aggregation [30-32]. We wanted to determine
114 how the levels of these associated Hsp40s changed as a function of tau seeding activity. Many of the
115 Hsp40s including DnaJA1, DnaJC6, DnaJA2, DnaJB4 and DnaJA4 were associated at different levels
116 but the normalized signal remained flat as tau seeding increased with mouse age (Supplementary Fig.

117 1b). The normalized abundance for DnaJC5 increased 10-fold over this window (Supplementary Fig. 1b).
118 For DnaJB6 and DnaJB1, we observed a 2-fold and 3-fold decrease in normalized abundance,
119 respectively (Supplementary Fig. 1b), while for DnaJC7 we found a 5-fold decrease in its normalized
120 abundance as tau seeding increased (Fig. 1a and Supplementary Fig. 1b). These data indicate that while
121 many Hsp40s can bind tau independent of seeding capacity some may have selectivity for different
122 conformations of tau and can discriminate between native vs aggregation-prone conformations. We were
123 intrigued by the behavior of DnaJC7, which is not known to bind substrates nor has it been implicated
124 directly in aggregation processes. We first tested whether DnaJC7 binding to tau can be directly detected
125 by western blot following IP from PS19 mouse brain tissues expressing human 1N4R tau [33]. DnaJC7
126 was immunoprecipitated from PS19 mouse brain lysates using an anti-DnaJC7 antibody or an IgG
127 isotype as a negative control. Immunoblotting revealed that tau co-immunoprecipitates with DnaJC7 while
128 no signal was observed in the negative control (Fig. 1b and supplementary Fig. 1c).

129
130 We then carried out the DnaJC7 knock-out experiment in tau biosensor cells to determine if the loss of
131 the tau:DnaJC7 interaction could change tau seeding activity in cells. Four CRISPR, guide RNAs
132 (gRNAs) targeting DnaJC7 (Supplementary Table 1) were used as a cassette to disrupt the DnaJC7 gene
133 in the HEK293 tau biosensor line [34]. And in parallel, a non-targeting gRNA sequence was used as a
134 negative control. Western blot of cell lysates was used to confirm the knock-out of DnaJC7
135 (Supplementary Fig. 1d). Compared with the negative control, we observed a noteworthy 4-fold increase
136 in tau seeding capacity in DnaJC7 knock-out cells induced by tau fibrils (Fig. 1c). Our *ex vivo* tau:DnaJC7
137 binding data and DnaJC7 knock-out effects on tau seeding in cells suggest that DnaJC7 could play a
138 crucial role in preventing tau aggregation *in vivo*.

139
140 **DnaJC7 binds tauRD through the R1R2 inter-repeat element.**

141 We first employed binding assays and structural approaches to determine how DnaJC7 directly interacts
142 with tauRD to influence its aggregation (Fig. 2a). DnaJC7 encodes three TPR domains (TPR1, TPR2a
143 and TPR2b) followed by a C-terminal J-domain. The 34-residue TPR motif is composed of a two-helix
144 bundle. Tandem TPR motifs form a ubiquitous protein interaction module that binds to peptides via a

145 canonical binding groove (Fig. 2a). We used a combination of microscale thermophoresis (MST) binding
146 measurements, solution NMR and crosslinking mass spectrometry (XL-MS) to probe how DnaJC7
147 interacts with wild-type tauRD (WT tauRD) and a frontotemporal dementia disease-associated P301L
148 mutant (P301L tauRD) (Fig. 2a). To investigate whether DnaJC7 directly binds to tauRD, we used MST
149 to measure binding affinity between DnaJC7 and WT tauRD or P301L tauRD derivatized with a cyanine
150 dye (Cy5-NHS-ester) (Fig. 2b and Supplementary Fig. 2a). Our measurements revealed that DnaJC7
151 binds to WT tauRD with $2.2 \pm 0.37 \mu\text{M}$ binding affinity while P301L tauRD bound with a three-fold lower
152 binding affinity relative to WT tauRD ($6.2 \pm 1.4 \mu\text{M}$). The P301L mutation is located in a conserved β -
153 hairpin motif just upstream of the $^{306}\text{VQIVYK}^{311}$ amyloid motif [35]. Prior work from our group has shown
154 that this mutation preferentially unfolds this structural motif to drive exposure of $^{306}\text{VQIVYK}^{311}$ that
155 promotes aggregation [36]. While other chaperones, including Hsc70/Hsp70, Hsp90, and Hsp40s, have
156 been shown to bind to $^{306}\text{VQIVYK}^{311}$ to suppress tau aggregation [31, 37], it is surprising that unfolding of
157 this motif in the mutant decreases affinity for DnaJC7.

158
159 To probe the domain interactions between DnaJC7 and tauRD in more detail, we employed XL-MS to
160 map intermolecular sites of interaction. XL-MS provides direct binary interaction pairs between residues
161 within a structure while also identifying binding contacts in protein complexes in a resolution range of 7–
162 30 Å [38]. The pre-formed complexes were reacted with disuccinimidyl suberate (DSS), quenched, and
163 hetero-dimer bands corresponding to the complex excised from an SDS-PAGE gel. The samples were
164 processed to isolate crosslinked peptides (see methods) and the peptides were analyzed by mass
165 spectrometry to identify the crosslink pairs using our established XL-MS pipeline (Supplementary Data
166 2) [39]. We only considered crosslink pairs with high score cut-offs that occurred across replicate
167 samples. We identified four crosslinks between K280, K281, and K311 of WT tauRD and K254 and K306
168 of DnaJC7 (Fig. 2c and Supplementary Fig. 2b). The tauRD crosslinks localize predominantly to the inter-
169 repeat regions that span the repeat 1 and 2 interfaces (herein R1R2) and include the $^{275}\text{VQIINK}^{280}$ amyloid
170 motif (Fig. 2c and Supplementary Fig. 2b), with one crosslink also localizing to the repeat 2 and 3 interface
171 (herein R2R3) in proximity to the $^{306}\text{VQIVYK}^{311}$ amyloid motif. Mapping these crosslinks onto a homology
172 model of DnaJC7, built using Rosetta [40], reveals that the K254 and K306 crosslinks are located in the

173 peptide binding groove in TPR2b (Fig. 2d; yellow spheres). Nearly identical crosslink patterns were
174 identified between P301L tauRD:DnaJC7 (Fig. 2c). Like the homologous ³⁰⁶VQIVYK³¹¹, ²⁷⁵VQIINK²⁸⁰ is
175 also important for tau assembly and fibrillization [35] and chaperones, including DnaJA2 and Hsp70, have
176 been shown to recognize these two amyloid motifs [31]. Our data support that DnaJC7 interacts with tau
177 via a defined TPR-based interaction, utilizing a peptide binding groove to recognize elements that include
178 the amyloid motifs.

179
180 To validate the tauRD region involved in binding to DnaJC7, we acquired 2D ¹H-¹⁵N HSQC spectra of ¹⁵N
181 tauRD alone and titrated with DnaJC7. TauRD assignments were transferred from previously published
182 data [41] (Supplementary Fig. 2c). The addition of DnaJC7 to the ¹⁵N tauRD revealed concentration-
183 dependent chemical shifts as highlighted by changes at Q276, L282, K290 (Fig. 2e; inset). Systematic
184 plotting of all chemical shift perturbations (CSPs) revealed changes that localized to the R1R2 element
185 extending through R2 and were consistent with the XL-MS site identification (Fig. 2f). Protein-protein
186 interactions generally only occur on non-buried surface; as such, we speculate that the identified inter-
187 repeat elements are likely more solvent exposed. To identify solvent exposed regions in tauRD, we
188 employed CS-Rosetta [42] guided by tauRD chemical shifts to produce an ensemble of conformations
189 that are consistent with SAXS-derived sizes (Fig. 2g). By calculating the solvent exposure of each
190 interface element in the ensemble and normalizing to the unfolded state, we revealed that the R1R2
191 element is on average more solvent-exposed (Fig. 2h; colored in red/green). We show a representative
192 model of tauRD colored by the repeat domain to highlight the preferential exposure of the R1R2 elements
193 (Fig. 2i; interface of red/green) which are compatible with NMR-based CSPs on tauRD in response to
194 DnaJC7 binding (Fig. 2j).

195
196 **Pathogenic mutations in tau modify its conformation and recognition by DnaJC7.**

197 While our initial data support that DnaJC7 can bind and modify aggregation of tauRD, our IP data support
198 that DnaJC7 can recognize full-length tau and may have binding preference for natively folded
199 conformations of tau. To gain insight into how DnaJC7 binds to full-length 2N4R WT and P301L tau, the
200 binding mode of interaction between tau and the chaperone, and possible changes in tau conformation

201 in response to pathogenic mutations we again employed binding assays and XL-MS. For the crosslinking
202 analysis, we first interpreted intramolecular crosslinks for WT and P301L tau, followed by analysis of
203 contacts derived from the WT tau:DnaJC7 and P301 L tau:DnaJC7 complexes.

204
205 Using MST, we determined that DnaJC7 binds to full-length tau with $\sim 471 \pm 53.5$ nM affinity (Fig. 3a and
206 Supplementary Fig. 3a), nearly 5-fold tighter than WT tauRD. We speculated that the N-terminus (N-term,
207 residues 1-243) could independently contribute to the binding affinity, but binding measurements for the
208 N-terminal fragment alone revealed an affinity of 17 ± 3.9 μ M (Supplementary Fig. 3a). These data hinted
209 at possible cooperativity between the N-terminus and the repeat domain. To further corroborate this
210 observation, we measured the affinity for the full-length P301L tau mutant and DnaJC7 and determined
211 the affinity to be 8.3 ± 2.2 μ M which is nearly 20-fold lower than WT (Fig. 3a and Supplementary Fig. 3a).
212 Taken together, DnaJC7 binds full-length tau with nanomolar affinity and pathogenic mutations in full-
213 length tau dramatically decrease affinity to levels similar to WT and P301L tauRD. Consistent with this
214 idea, we also measured binding of DnaJC7 for a tau monomer seed [28] and find that it binds weakly with
215 15.5 ± 2.2 μ M affinity (Supplementary Fig. 3a). These data suggest that DnaJC7 preferentially binds to a
216 natively folded conformation of tau with high affinity in which the N-terminus and the repeat domain are
217 more stably associated. We hypothesize that the P301L tau mutation shifts the conformation towards an
218 aggregation-prone seeding conformation which has lower affinity for DnaJC7.

219
220 To test this idea, we first employed XL-MS to probe the how conformational changes in WT and P301L
221 tau could dictate the observed differences in affinity for DnaJC7. WT and P301L tau were reacted with
222 DSS or the zero length crosslinker 4-(4,6-Dimethoxy-1,3,5-triazin-2-yl)-4-methylmorpholinium (DMTMM)
223 at 25°C and 50°C, quenched, and the crosslinked monomer band were extracted from SDS-PAGE gels
224 (Supplementary Fig. 3b). We employed these two temperatures to probe the stability of the interactions
225 in response to unfolding. The crosslinks were processed through our XL-MS pipeline as replicates and
226 only high scoring pairs present across replicate datasets were considered (Supplementary Data 2). We
227 identified 103 and 41 consensus crosslinks at 25°C for WT tau using the DSS and DMTMM chemistries,
228 respectively. The reactions performed at 50°C for WT tau yielded a nearly two-fold drop in DSS crosslinks

229 (Fig. 3b; 60 pairs), while the number of DMTMM pairs remained flat at 47 crosslinks (Fig. 3d). For P301L
230 tau, we identified 81 and 82 consensus crosslinks using the DSS and DMTMM chemistries at 25°C,
231 respectively. In contrast to the WT tau datasets, at 50°C, the numbers of consensus crosslinks for P301L
232 tau remained relatively flat with 79 and 68 for the DSS and DMTMM chemistries, respectively. Each
233 crosslinking chemistry captures different types of interactions; DSS traps contacts between primary
234 amines (i.e. lysines) while DMTMM traps contacts between primary amines (i.e. lysines) and carboxylic
235 acids (i.e. aspartic and glutamic acids). We surmised that DSS would predominantly capture contacts
236 within the basic repeat domain, while the DMTMM chemistry would trap interactions between the acidic
237 termini and the basic repeat domain. Indeed, DSS captures more contacts within the repeat domain
238 compared to the N-terminus for both WT and P301L tau (Fig. 3b and Supplementary Fig. 3c). We also
239 observed that in WT tau, we captured many more DSS crosslinks in the repeat domain compared to
240 P301L tau at 25°C. Increasing the temperature reduced the number of repeat domain crosslinks by two-
241 fold in WT and only reduced them by 25% in P301L tau (Fig. 3b). This difference is most dramatic when
242 comparing the number of crosslinks from the 25°C experiment in proximity to residue 301. In WT tau, we
243 observe twelve contacts that are completely missing in the P301L tau mutant (Fig. 3c). Consistent with
244 domain charge distributions, in the DMTMM reactions, we detect overall more contacts between the
245 acidic N-terminus and the basic repeat domain and much less within the basic repeat domain
246 (Supplementary Fig. 3d). In P301L tau, we observe nearly 40 crosslinks involving the N-term at 25°C and
247 the number drops nearly two-fold at higher temperature. In contrast, we observe less N-terminal
248 crosslinks in WT tau and it appears relatively insensitive to temperature (Fig. 3d). This is highlighted by
249 the dramatic difference in the number of contacts when comparing P301L and WT tau. Taken together,
250 these XL-MS experiments reveal large differences in distribution of contacts within WT and P301L tau
251 underscored by changes in repeat domain in response to pathogenic mutations (Fig. 3c). This is
252 consistent with our previous work on tauRD [36] and expands the conformational changes in full-length
253 tau to also include perturbations of long-range contacts between the acidic N-terminal contacts with the
254 more basic proline-rich and repeat domains.

255

256 Our data support that the P301L mutation significantly changes the dynamics of the repeat domain in
257 proximity to the mutation and also affects the overall dynamics of the acidic N-terminus with respect to
258 the repeat domain. We surmise that changes in tau conformation impact the different affinities between
259 WT and P301L tau towards DnaJC7. It is unclear how dynamics of the tau N-terminus, alter binding to
260 DnaJC7? We again turned to XL-MS to probe the WT tau:DnaJC7 and P301L tau:P301L complexes to
261 gain insight into which domains mediate the interaction. As in prior experiments for tauRD:DnaJC7, pre-
262 formed complexes between WT tau:DnaJC7 and P301L tau:DnaJC7 were reacted with DSS, quenched,
263 and the bands corresponding to the heterodimer complex extracted from SDS-PAGE gels. The samples
264 were processed, and analyzed by LC-MS/MS using our XL-MS pipeline to identify consensus crosslinks
265 across replicates with high score cutoffs (Supplementary Data 2). Similarly to how tauRD binds to
266 DnaJC7, the major binding site that binds WT and P301L tau on the chaperone is TPR2b (Fig. 3f).
267 However, partitioning the identified TPR2b crosslinks to tau revealed data consistent with the P301L
268 mutant tau being more unfolded (Fig. 3f). Although the overall numbers of tau crosslinks to the TPR2b
269 domain were similar between WT and P301L tau, they appear to partition differently across P1/P2 sites
270 in the proline-rich domain and the repeat domain in tau (Fig. 3g). In WT tau, we observe nearly five-fold
271 less crosslinks between TPR2b and R1R2 and two-fold more crosslinks between TPR2b and P1/P2 sites
272 compared to P301L tau. This is because DnaJC7 binds to R1R2 and buries this element in the binding
273 pocket which yields fewer crosslinks.

274
275 Finally, analysis of tau intramolecular contacts from the XL-MS datasets derived from WT tau:DnaJC7
276 complexes showed a complete absence of long range contacts with the N-terminus, while in the P301L
277 tau:DnaJC7 complex these persist, suggesting that DnaJC7 binds preferentially to the folded
278 conformation of WT tau (Supplementary Fig. 3e). Thus, it appears that a more stable interaction between
279 the N-terminus and the repeat domain observed in WT tau preferentially leads to higher affinity binding,
280 resulting in exposure of the P1/P2 sites and burial of the R1R2 in the tau:DnaJC7 binding interface.
281 Consistent with this observation, both the similarly “unfolded” WT and P301L tauRD have comparable
282 affinity to DnaJC7 as the aggregation-prone full-length P301L tau. To further corroborate our findings, we
283 measured the frequency of total chemical modifications (i.e. monolinks and loop links) as a proxy for

284 changes in solvent exposure. We found that the P1/P2 region has a six-fold higher rate of modification
285 in WT tau:DnaJC7 compared to WT tau alone (Supplementary Fig. 3f). This region is comparably
286 modified in P301L tau and P301L tau:DnaJC7 but approximately two-fold lower than in WT tau:DnaJC7
287 (Supplementary Fig. 3f). In contrast, we observed that the modification frequency in the R1R2 interface
288 region dropped two-fold in the WT tau:DnaJC7 complex relative to the tau alone (Supplementary Fig. 3f).
289 These data reaffirm our intermolecular crosslink data on the complexes and support that P301L tau is
290 more unfolded. Taken together, these data suggest that the N-terminus plays an important role in
291 defining the topology of the native tau “fold,” which is dramatically altered by pathogenic mutations. While
292 the tauRD fragment is a good proxy for aggregation, it lacks the regulatory elements that define the native
293 conformation observed in full-length tau.

294

295 **DnaJC7 efficiently inhibits aggregation of tau *in vitro*.**

296 While DnaJC7 appears to impact tau seeding in cells and binds native folded tau with high affinity *in vitro*,
297 we wanted to test whether DnaJC7 alone can control tau aggregation *in vitro*. We monitored tau
298 aggregation using a Thioflavin T (ThT) fluorescence aggregation assay to determine the capacity of
299 DnaJC7 to suppress the formation of tau fibrils when tau monomer is induced with substoichiometric
300 amounts of recombinant isolated tau monomer seeds [28]. 4.4 μ M wild-type tau monomer was incubated
301 with 50 nM tau monomer seeds in the presence of different concentrations of DnaJC7, including controls
302 to monitor the behavior of each component (i.e. tau alone, tau monomer seeds alone, DnaJC7 alone;
303 see methods for details). We found that equimolar concentrations of 4.4 μ M DnaJC7 (1:1) yielded efficient
304 suppression of seeded 4.4 μ M tau aggregation. Further, we found that even substoichiometric (44:1)
305 amounts of 0.1 μ M DnaJC7 reduced ThT signal by 20% over the time course (Fig. 4a). Consistent with
306 the ThT signal, at the end of the time course, we observed tau fibrils in reactions without DnaJC7 as
307 determined by TEM, while fibrils were not detected in the presence of DnaJC7 (Fig. 4a). Parallel
308 experiments carried out with P301L tau revealed that DnaJC7 has a weaker capacity to suppress seeded
309 4.4 μ M tau aggregation, highlighted by the absence of ThT signal reduction at the 44:1 ratio, which is
310 consistent with lower affinity for this interaction (Fig, 4b).

311

312 To confirm the presence of tau aggregates in our *in vitro* samples, we employed an in-cell tau biosensor
313 assay to detect the seeding capacity of exogenously delivered tau using FRET [29]. Endpoints from our
314 *in vitro* aggregation experiment (above) were transduced into biosensors cells, including negative and
315 positive controls, and measured FRET to quantify the amount of tau aggregates in each sample. Our
316 positive (recombinant tau fibrils) and negative (lipofectamine alone) controls yielded $76.5 \pm 1.4\%$ and
317 $0.16 \pm 0.16\%$ FRET signal, respectively. Consistent with the ThT assays, transduction of the *in vitro*
318 incubated samples, revealed a reduction in seeding capacity as a function of DnaJC7 concentration (Fig.
319 4c,d and Supplementary Fig. 4a). In the samples without DnaJC7, we detected $59.4\% \pm 8.7$ of the cells
320 with aggregates and at 3:1 and 1:1 tau:chaperone ratios, the number of cells with aggregates decreased
321 by two-fold over the course of the experiment to $27.1\% \pm 2.9$ and $26.9\% \pm 4.2$, respectively. Parallel seeding
322 experiments with the P301L tau samples across a range of DnaJC7 concentrations revealed nearly
323 $69.7\% \pm 5.3$ of cells contained aggregates in the absence of DnaJC7. To achieve two-fold inhibition of tau
324 seed formation over six days, 1:1 ratios of P301L tau:DnaJC7 were required ($34.2\% \pm 2.8$), consistent with
325 our finding that DnaJC7 has a lower affinity for P301L tau than WT tau. We also examined the effects of
326 a canonical co-chaperone, DnaJA1, on tau aggregation. DnaJA1 showed only a minor effect of tau
327 aggregation relative to DnaJC7 (Supplementary Fig. 4b). Our data support that DnaJC7 is a potent
328 suppressor of tau aggregation by efficiently binding to natively folded conformations of tau.

329

330 **Individual TPR domains bind tightly but do not suppress tau aggregation.**

331 In general, TPR domains, like the three found in DnaJC7, can be seen as scaffolds to mediate protein
332 interactions. Our XL-MS data support that TPR2b in DnaJC7 is the main domain that recognizes tau. To
333 understand how DnaJC7 regulates tau aggregation, we set out to determine whether individual TPR
334 domains (TPR1₂₀₋₁₅₆, TPR2a₁₄₁₋₂₇₀, and TPR2b₂₅₅₋₃₇₀) or the J-domain₃₈₀₋₄₉₄ can bind and suppress tau
335 aggregation (Fig. 5a). Each individual domain was expressed recombinantly and purified using a two-
336 step purification protocol (methods). We first used the MST binding assay to determine the affinity for
337 each domain to full-length tau. We found that the J-domain has weak binding affinity to WT and P301L
338 tau (Fig. 5b; $8.2 \pm 0.7 \mu\text{M}$ and $28.2 \pm 3.3 \mu\text{M}$, respectively; Supplementary Fig. 5a). In contrast, TPR1

339 and TPR2b have high binding affinities towards WT tau (Fig. 5b; 84 ± 6 nM and 75 ± 5 nM, respectively;
340 Supplementary Fig. 5a) that are nearly eight-fold tighter than full-length DnaJC7. Similarly, TPR2a also
341 showed a greater than two-fold tighter binding to WT tau compared to full-length DnaJC7 (Fig. 5b and
342 Supplementary Fig. 5a). We reasoned that the more nonpolar binding groove of TPR2a could impact
343 binding to tau, given its distinct patterning from the other domains (Fig. 5c). For P301L tau binding, we
344 observed a similar increase of binding ability of individual TPRs with a greater than 12-fold increase in
345 binding affinity relative to full-length DnaJC7 (Fig. 5b and Supplementary Fig. 5a).

346
347 To identify how each individual domain interacts with tau, we again employed XL-MS. Briefly, complexes
348 between the individual DnaJC7 domains and tau were pre-formed, reacted with DSS, quenched, and the
349 species resolved by SDS-PAGE to extract bands corresponding to the hetero-dimer (Supplementary Fig.
350 5b). Samples were processed, analyzed by mass spectrometry, and crosslinked sites were identified
351 using our XL-MS pipeline. The identified crosslinks between tau and each single TPR domain imply that
352 the individual domains bind in a largely distributed fashion, suggesting a loss of specificity in tau binding
353 relative to full-length DnaJC7 (Supplementary Fig. 5c). Comparison of the surface properties of the
354 binding grooves on TPR1, TPR2a, and TPR2b reveals that their binding grooves are similar with some
355 differences (Fig. 5c). Notably, TPR1 and TPR2b encode more basic residues while TPR2a is more acidic
356 (Fig. 5c). Importantly, the individual TPR domain crosslink experiments show that they each are capable
357 of binding to tau. However, XL-MS revealed that only the TPR2b:tau interaction recapitulates similar
358 crosslink patterns observed for TPR2b in the context of full-length DnaJC7 (Supplementary Fig. 5c). Our
359 data suggest that individual TPR domains bind tightly in a distributed binding mode dictated by TPR2b
360 contacts, suggesting that the arrangement of the three domains within full-length DnaJC7 and their
361 surface properties help define recognition specificity to bind a natively folded conformation of tau.

362
363 Given the high-affinity interaction between individual TPR domains and tau, we tested whether individual
364 TPR domains can modulate tau aggregation via the ThT fluorescence aggregation assay. In these
365 experiments, we incubated $4.4 \mu\text{M}$ full-length tau with 50 nM tau monomer seeds and compared the
366 effects of the addition of equimolar amounts of each TPR domain, or combining all three individual

367 domains, to the full-length DnaJC7 by monitoring tau aggregation for 50 hours (Fig. 5d and
368 Supplementary Fig. 5d). The endpoint of the curves showed that tau aggregates upon the addition of tau
369 monomer seeds and that the addition of DnaJC7 completely abolishes tau aggregation. Unexpectedly,
370 none of the individual TPR domains modified tau aggregation significantly and TPR1₂₀₋₁₅₆ even yielded a
371 slight increase in aggregation. However, the addition of all three TPRs restores the capacity to inhibit
372 tau aggregation (Fig. 5d and Supplementary Fig. 5b). Thus, while each TPR binds tightly to tau, single
373 domain binding is insufficient to modulate tau aggregation. These results strongly suggest that DnaJC7
374 uses a specific domain-domain co-occurrence conformation between three TPR domains to mitigate tau
375 aggregation.

376

377 **DnaJC7 recognizes local structures important for the regulation of tau aggregation.**

378 Our high-resolution NMR data and XL-MS experiments on the tau:DnaJC7 complex revealed that
379 DnaJC7 binds to a small structural element, R1R2, through a binding groove in TPR2b. Recent work
380 from our lab showed that these structural elements, including R1R2, can adopt transient β -hairpin
381 conformations to bury amyloid motifs and that pathogenic mutations perturb these hairpin structures to
382 expose amyloid motifs, thus promoting aggregation [36]. Given that DnaJC7 appears to interact with this
383 structural element, we wondered whether a P270S mutation in the β -turn-stabilizing P-G-G-G motif in the
384 R1R2 element would alter binding affinity to the chaperone. Using MST, we found that P270S tauRD
385 does not bind to DnaJC7 (Supplementary Fig. 6a), indicating that this region is important for DnaJC7
386 recognition. Further, a ThT fluorescence aggregation assay revealed that DnaJC7 can efficiently control
387 aggregation of WT tauRD but has little to no effect on suppressing P270S tauRD aggregation
388 (Supplementary Fig. 6b-d), consistent with our binding measurements. These data strongly support that
389 the R1R2 element is recognized by DnaJC7 in a native-like collapsed conformation.

390

391 We used computational modeling to gain more insight into how DnaJC7 can bind the R1R2 element. We
392 carried out unbiased coarse-grained docking with DnaJC7 against an ensemble of R1R2 and R2R3
393 peptides derived from our prior CS-Rosetta tauRD calculations. Our ensemble sampled a diversity of
394 conformations to produce 5000 models of DnaJC7 bound to each sequence followed by full-atom

395 refinement to calculate binding energies (Fig. 6a and Supplementary Fig. 6e). We found that many of the
396 predicted binding modes do not yield favorable energetics for binding. However, partitioning the
397 structures according to geometric compatibility with our crosslinks revealed R1R2:DnaJC7 complexes
398 with energetically favorable binding modes (Fig. 6b). In fact, simply restricting the models to only ones
399 that are consistent with crosslinks between K280 in R1R2 and K254 on TPR2b revealed a set of
400 structures with favorable binding energies. Mapping our crosslink data onto one of these models reveals
401 conformations consistent with our experiments. The R1R2 element can be stabilized in a collapsed
402 conformation, trapping contacts between K267 and K280/K281 (Fig. 6c; orange dashed lines). Further,
403 K280/K281 forms contacts with K254/K306 of TPR2b (Fig. 6c; yellow dashed lines). The R1R2 element
404 binds to DnaJC7 in a sequence conserved binding groove (Fig. 6d) in a binding mode that is also
405 compatible with the CSP experiments (Fig. 6e), suggesting congruency across several experiments to
406 explain how the TPR2b in DnaJC7 can recognize a natively folded conformation of the R1R2 peptide.

407
408 Our data predict that the WT R1R2 peptide alone could bind to DnaJC7 and that a P270S R1R2 mutant,
409 which is more unfolded, would not. Though initial efforts to measure the affinity between the peptides and
410 DnaJC7 were unsuccessful, we turned to aggregation experiments to ask if the addition of WT or P270S
411 R1R2 peptides could alter the ability of DnaJC7 to modulate aggregation of tauRD in a ThT fluorescence
412 aggregation assay (Fig. 6f). In the presence of P270S R1R2, we observed no inhibition of DnaJC7
413 activity (Fig. 6g and Supplementary Fig. 6f). However, the addition of the WT R1R2 peptide allows only
414 $65.3 \pm 5\%$ recovery of DnaJC7 tau aggregation suppression activity (Fig. 6g and Supplementary Fig. 6f).
415 These data suggest that the WT R1R2 peptide can bind to TPR2b to prevent tau binding to DnaJC7
416 leading to an increase in tau aggregation but the P270S R1R2 peptide cannot. These data suggest that
417 DnaJC7 influences tau aggregation by binding to specific elements in tau in a conformationally dependent
418 manner.

419
420 **Discussion**
421 How tau changes shape to promote the formation of pathogenic species underlying disease remains an
422 important biological question [43, 44]. In the time since the discovery that tau deposits as fibrillar

423 structures in human disease, we have gained insight into the genetics of the disease and uncovered
424 mutations in tau that cause early-onset dominantly inherited tauopathies. Structural insight into how tau
425 mutations change its shape is an important proxy for understanding how tau can adopt pathogenic
426 conformations. We previously used a multidisciplinary approach to study the structure of a wild-type tau
427 monomeric pathogenic seed and revealed local conformations within tau that underly amyloid motifs [28].
428 More recently, we compared the unfolding profiles of WT and P301L tauRD using XL-MS and revealed
429 that pathogenic mutations promote unfolding of the repeat domain in proximity to the P301L mutation,
430 preferentially exposing the ³⁰⁶VQIVYK³¹¹ amyloid motif [28, 36]. In this study, we compared full-length
431 WT and P301L tau using two parallel crosslinking chemistries to highlight how pathogenic mutations
432 unfold the repeat domain in proximity to the P301L mutation, which impacts the folding of the N-terminus.
433 Our data suggest that tau undergoes discrete conformational changes that underlie disease
434 pathogenesis. While mutations in tau are predominantly linked to Frontotemporal dementia, we propose
435 that similar conformational changes that expose amyloidogenic motifs must underlie WT tau conversion.
436 However, the means through which this happens remains unknown, though cofactors have been
437 proposed as possible drivers of WT tau aggregation. Amyloid motifs central to aggregation are engaged
438 in stabilizing contacts and lead to distinct topologies for fibrils from different diseases [45-48]. Our model
439 predicts that local engagement of the amyloid motifs inhibits aggregation. The early conformational
440 changes enabled by cofactor binding or mutations uncover the amyloid motifs allowing them to form
441 unique contacts that are on-path to fibril formation.

442
443 Our data support that DnaJC7 preferentially binds natively folded forms of tau over more unfolded
444 aggregation-prone mutant forms and tau monomeric seeds derived from WT tau. To our surprise,
445 DnaJC7 binds to WT tau with 0.4 uM affinity, which is tighter than most chaperone:substrate interactions
446 [31, 49, 50]. However, the general role of chaperones is to recognize nonpolar sequences in proteins that
447 are typically buried in protein cores to promote their folding into functional, folded conformations [1]. Given
448 this high affinity, what is the role of DnaJC7 in tau binding? While many chaperones, including Hsp70s
449 and other Hsp40s, bind to tau via its encoded amyloid motifs to prevent aggregation, the capacity of these
450 chaperones to suppress tau aggregation is orders of magnitude less efficient [31, 51, 52]. In contrast,

451 DnaJC7 appears to recognize a more natively folded conformation of tau. Coupled with its high affinity
452 for tau, this aspect likely underlies DnaJC7's efficient capacity to limit tau aggregation even on long time
453 scales. Finally, our comparison of DnaJC7 activity against WT and P301L tau reveals a dramatic
454 difference in affinity, likely dictated by changes in tau conformation induced by the pathogenic P301L
455 mutation. Indeed, many pathogenic mutations linked to tau localize to our identified DnaJC7 binding
456 regions, suggesting that DnaJC7 has a reduced capacity to prevent aggregation of more aggregation-
457 prone and disease-associated variants of tau. This perhaps implicates DnaJC7 as an evolved binding
458 partner for tau that may play a role in transporting native conformations of tau by stabilizing aggregation-
459 resistant conformations similarly to how DnaJC7 sequesters the CAR transcription factor in the cytosol.
460 Future cellular experiments are required to reveal the central role of DnaJC7 in tau biology.

461
462 Work from Reagan *et al* on TPR domains has defined simple rules that set the basis for how these
463 protein-binding modules interact with peptides. However, there exists a large diversity of TPR-containing
464 proteins in mammalian cells and while these rules apply to some, it is not clear how TPR sequence
465 divergence broadens their capacity to bind structured peptides. In the context of co-chaperones, TPR
466 domains have previously been proposed to recognize conserved EEVD C-terminal tails on Hsp70 and
467 Hsp90 chaperones [53]. For example, HOP uses two of its three TPR modules to simultaneously bind to
468 the acidic tails of these proteins and thus bring them together [54]. Details for this mechanism are not
469 clear, but it is thought that HOP may promote the transfer of the substrate from one chaperone to the
470 other. However, the DnaJC7 co-chaperone has not been implicated in binding to protein clients directly
471 [55]. While the three TPR domain architecture of DnaJC7 is similar to HOP, DnaJC7 also encodes a C-
472 terminal J-domain. Mechanistic insight on DnaJC7 is sparse in the literature, though peptide binding
473 experiments have shown that DnaJC7 can bind Hsp70/Hsp90-derived EEVD sequences with weak
474 affinity [56]. However, alignment of the HOP and DnaJC7 sequences reveals little similarity, including
475 sequence changes in residues on TPRs important for recognition of EEVD-containing peptides. High
476 sequence conservation of the DnaJC7 TPR domains in metazoans suggests that this chaperone may
477 have additional functions divergent from HOP. It is possible that DnaJC7 can bind directly to substrates
478 through the TPR domains (tau via TPR2b) and that it can also recruit Hsp70 and Hsp90 through their

479 acidic tails to localize substrates to these chaperones. Hsp90 and Hsp70 are both known to be associated
480 with tau [52, 57, 58]. Thus, in the context of DnaJC7, it is possible that direct substrate binding via TPR
481 domains allows the C-terminal J-domain to recruit Hsp70 to promote substrate transfer. Resolving the
482 potential dual nature of substrate binding and chaperone recruitment will require additional experiments,
483 but this complex model highlights a more nuanced cooperation of chaperones in networks to maintain a
484 healthy proteome.

485

486 **Acknowledgements**

487 This work was supported by grants to L.A.J from the Marie Effie Cain Endowed Scholarship, a Chan
488 Zuckerberg Initiative Collaborative Science Award (2018-191983) and a Bright Focus Foundation grant
489 (A2019060). We appreciate the help of the Molecular Biophysics Resource core, Structural Biology
490 Laboratory, Biomolecular Nuclear Magnetic Resonance Facility, Cryo-Electron Microscopy Facility and
491 Proteomics Core Facility at the University of Texas Southwestern Medical Center. We thank Dailu Chen
492 for helping in analysis of the XL-MS monolink and looplink data. We also thank members of the
493 Joachimiak lab for reading and providing critical comments on the manuscript.

494

495 **Author Contributions**

496 Z.H. and L.A.J. conceived and designed the overall study. V.A.P. performed the immunoprecipitations
497 and seeding experiments in WT and KO biosensor cells. Z.H., P.M.W. and O. K. purified all the
498 recombinant proteins. Z.H. performed *in vitro* protein binding and aggregation assays. Z.H and B.D.R
499 acquired and analyzed the NMR spectra. Z.H. and P.M.W. performed the crosslink mass spectrometry
500 experiments and analysis. Z.H. performed the ROSETTA simulations. A.M.O. performed the in cell
501 seeding experiments. B.D.R performed the TEM. Z.H. and L.A.J. wrote the manuscript, and all authors
502 contributed to its improvement.

503

504 **Competing interests**

505 The authors declare no competing interests.

506

507 **Data availability**

508 The data sets generated during and/or analysed during the current study are available from the
509 corresponding authors on reasonable request.

510

511

512 **Methods**

513 **Isolation of tau from PS19 mouse brains**

514 Soluble tau species were immuno-purified from PS19 mouse brain using the HJ8.5 anti-human tau
515 antibody [28]. Briefly, 0.5g brain tissues from week 1, 2, 3, 4, 5 and week 6 mouse were gently dounce-
516 homogenized in 1XPBS buffer in the presence of protease inhibitors and centrifuged at 21,000 RCF for
517 15 minutes at 4°C to remove the debris. The supernatants were mixed with HJ8.5 (1:50, m/m) and 50%
518 slurry protein G-agarose beads (1:5, v/v) and incubated at 4°C overnight. Next day, the binding reactions
519 was centrifuged at 1000 RCF for 3 minutes and the pellet was washed with Ag/Ab binding buffer (Thermo
520 Scientific) three times. The antibody bound tau was eluted in 100 µL low-pH elution buffer directly into 10
521 µL Tris-base pH 8.5 to neutralize the buffer. Elution was repeated once more with 50 µL elution buffer
522 into 5 µL Tris-base buffer pH 8.5 for a total volume 165 µL. Samples were further purified on a Superdex
523 200 Increase 10/300 GL on an AKTA FPLC. Fractions containing tau were determined using western blot
524 and the pooled samples were quantified with a Micro BCA assay (Thermo Scientific), flash frozen in liquid
525 nitrogen and stored at -80°C.

526

527 **Mass spectrometry analysis of mouse tau samples**

528 The purified tau samples were denatured with 8M urea, reduced with 2.5mM TCEP, alkylated with 5mM
529 iodoacetamide in the dark for 30 minutes and the urea diluted to 1M using 50mM ammonium bicarbonate.
530 Trypsin was added to 1:50 (m/m) (Promega) and incubated overnight at 37°C with 600 rpm shaking on a
531 thermomixer. 2% (v/v) formic acid was added to acidify the reaction and further purified by reverse-phase
532 Sep-Pak tC18 cartridges (Waters). The eluted peptides were quantified on a denovix nanospectrometer.

533 The dried samples were resuspended in water/acetonitrile/formic acid (95:5:0.1, v/v/v) to a final
534 concentration of approximately 0.5 µg/µL. 2 µL each will be injected into Eksigent 1D-NanoLC-Ultra
535 HPLC system coupled to a Thermo Orbitrap Fusion Tribrid system at the UTSW Proteomics core. The
536 data for each fraction were analyzed using the Proteome Discoverer Suite (Thermo) and searched
537 against the mouse proteome to identify hits. Only hits with PSM values of >5 were further considered.
538 The cumulative intensities for each hit were normalized to MAPT intensities. Final analysis focused on
539 all 47 members of the Hsp40 family. Hsp40 abundance was normalized to intensity values for 1N4R tau
540 according to the following equation $[I_{\text{Hsp40}}/I_{\text{tau}}]*100$.

541

542 **Co-immunoprecipitation of tau with DnaJC7**

543
544 Littermate wildtype and PS19 mouse brains weighing approximately 400 mg were Dounce homogenized
545 in 5 mL of TBS (10 mM Tris, 150 mM NaCl, pH 7.4). Homogenates were then clarified by centrifugation
546 at 4°C at a speed of 17,200 RCF for 15 minutes. The supernatant was then isolated. Total brain protein
547 concentrations were measured using the Pierce™ BCA Protein Assay Kit (ThermoFisher). For
548 immunoprecipitations, the magnetic Dynabeads™ Protein A Immunoprecipitation Kit (ThermoFisher) was
549 used following the standard protocol from ThermoFisher. 4 mg of anti-DnaJC7 antibody (Proteintech,
550 11090-1-AP) were conjugated to 50 µL total Dynabeads™ suspension overnight at 4°C with rotation.
551 Normal rabbit IgG (4 mg, Abcam, ab37415) was used for control immunoprecipitations. 300 µg of total
552 mouse brain protein was added to the antibody-conjugated Dynabeads™ and incubated at 4°C overnight.
553 After overnight incubation, the flow-through was collected after beads were isolated using a DynaMag™
554 Magnet. Following washes of the beads with Washing Buffer, proteins were incubated with 20 µL Elution
555 Buffer for 5 minutes at room temperature. Proteins were then eluted by collecting the supernatant after
556 beads were isolated using a DynaMag™ Magnet.

557 Immunoprecipitation elutions and flow-throughs, mouse brain homogenates, and recombinantly purified
558 2N4R tau and DnaJC7 samples were prepared in 1X (final) LDS Bolt™ buffer (Invitrogen) supplemented
559 with 10% β-mercaptoethanol and heated for 10 minutes at 98°C. The samples consisted of 10 µL of IP
560 elutions, 1% or 10% (Tau blot and DnaJC7 blot, respectively) of the total brain protein input into the IP,
561 1% or 10% (Tau blot and DnaJC7 blot, respectively) of the collected flow-through volume, and 50 ng of

562 recombinant Tau or DnaJC7. The proteins were resolved by SDS-PAGE using Novex NuPAGE pre-cast
563 gradient Bis-Tris acrylamide gels (4–12%) (Invitrogen). After gel electrophoresis, resolved proteins were
564 transferred onto Immobilon-P PVDF membranes (Millipore Sigma) using a Bio-Rad Trans-blot® semi-dry
565 transfer cell. After protein transfer, membranes were blocked in TBST buffer (10 mM Tris, 150 mM NaCl,
566 pH 7.4, 0.05% Tween-20) containing 5% non-fat milk powder (Bio-Rad). Membranes were then probed
567 with antibody in TBST containing 5% milk powder. The following antibodies were used for immunoblotting:
568 rabbit polyclonal anti-DnaJC7 (Proteintech, 11090-1-AP) at a 1:2000 dilution; rabbit polyclonal anti-tau
569 (Agilent, A002401-2) at a 1:3000 dilution; a secondary antibody that only recognizes native (non-
570 denatured) antibodies (Abcam, ab131366) at a 1:2000 dilution to minimize the detection of the heavy and
571 light chains from the antibody used in the immunoprecipitation when blotting for DnaJC7; and a
572 secondary donkey-anti-rabbit HRP-linked F(ab')₂ at a 1:8000 dilution (Cytiva, NA9340-1ML) when blotting
573 for tau.

574

575 **CRISPR/Cas9 knockout of DnaJC7 in tau biosensor cells**

576 Four human gRNA sequences per gene were selected from the Brunello library [59]. A single non-
577 targeting human gRNA sequence was used as a negative control. For all gRNA sequences not beginning
578 with guanine, a single guanine nucleotide was added at the 5'-end of the sequence to enhance U6
579 promoter activity. DNA oligonucleotides were synthesized by IDT DNA and cloned into the lentiCRISPRv2
580 vector [60] for lentivirus production. The plasmids for the four gRNAs for each gene were pooled together
581 and used to generate lentivirus.

582 Lentivirus was produced as described previously [61]. HEK293T cells were plated at a concentration of
583 100,000 cells/well in a 24-well plate. 24 hours later, cells were transiently co-transfected with PSP helper
584 plasmid (300 ng), VSV-G (100 ng), and gRNA plasmids (100 ng) using 1.875 µL of TransIT-293 (Mirus)
585 transfection reagent. 48 hours later, the conditioned medium was harvested and centrifuged at 1000 rpm
586 for five minutes to remove dead cells and debris. For transduction, 30 µL of the virus suspension was
587 added to HEK293T tau biosensor cells at a cell confluency of 60% in a 96-well plate. 48 hours post-
588 transduction, infected cells were treated with 1 µg/ml puromycin (Life Technologies, Inc.) and maintained

589 under puromycin selection for at least 10 days after the first lentiviral transduction before conducting
590 experiments.

591 592 **Flow Cytometry of tau biosensor cells**

593 Samples from immunoprecipitated mouse brain or ThT assay at T=0 (directly from the freezer) and T=6
594 days (end point of the aggregation experiment) were assayed for their seeding activity in HEK293T tau
595 biosensor cells. For the DnaJC7 KO and non-targeting control seeding experiments, HEK293T tau
596 biosensor cells with either a DnaJC7 KO or a non-targeting control were used. For all experiments, cells
597 were plated in 96-well plates at 20,000 cells per well in 100 μ L of media. 24 hours later, the cells were
598 treated with 50 μ L of a heparin-induced recombinant tau fibril dilution series. Prior to cell treatment, the
599 recombinant tau fibrils were sonicated for 30 seconds at an amplitude of 65 on a Q700 Sonicator
600 (QSonica). A three-fold dilution series of the sonicated fibril concentrations ranging from 100 nM to 15.2
601 μ M and a media control was added to the cells. 48 hours after treatment with tau, the cells were harvested
602 by 0.05% trypsin digestion and then fixed in PBS with 2% paraformaldehyde.

603 A BD LSRFortessa was used to perform FRET flow cytometry. To measure mCerulean and FRET signal,
604 cells were excited with the 405 nm laser and fluorescence was captured with a 405/50 nm and 525/50 nm
605 filter, respectively. To measure mClover signal, cells were excited with a 488 laser and fluorescence was
606 captured with a 525/50 nm filter. To quantify FRET, we used a gating strategy where mCerulean bleed-
607 through into the mClover and FRET channels was compensated using FlowJo analysis software. As
608 described previously [36]. FRET signal is defined as the percentage of FRET-positive cells in all analyses.
609 For each experiment, 10,000 cells per replicate were analyzed and each condition was analyzed in
610 triplicate. Data analysis was performed using FlowJo v10 software (Treestar).

611 612 **Protein expression and purification**

613 Wild-type and mutant tau or tauRD were purified from *E. Coli* BL21 (DE3) transformed with PET28b
614 plasmid using the same protocol as previously described [36]. N¹⁵ labeled human tauRD was expressed
615 in M9 medium supplemented with 2mM MgSO₄, 0.1mM CaCl₂, 0.4% (w/v) D-glucose, 0.0005% (w/v)
616 Thiamine, trace element and was purified with same procedure as unlabeled protein. The production of
617 tau seeds was carried out by incubating 16 μ M wild-type tau with 1:1 molar ratio of Heparin (AMSBio) for

618 1 hour at 37°C in 30 mM MOPS pH7.4, 50 mM KCl, 5mM MgCl₂ and 1 mM with DTT (MOPS buffer). The
619 tau:heparin reactions were injected onto a Superdex 200 Increase 10/300 GL (GE) in 1X PBS yielding a
620 peak that eluted around 1ml earlier than wild-type tau. The seeding activity was confirmed using tau
621 FRET biosensor cells.

622 The pMCSG7-DnaJC7 plasmid was a kind gift from Dr. Andrzej Joachimiak (Argonne National Lab).
623 Briefly, harvested cells were lysed by a pressure homogenizer in a buffer containing 50 mM Tris pH 7.4,
624 500 mM NaCl, 1 mM β-mercaptoethanol, 20 mM imidazole, 1 mM phenylmethylsulfonyl fluoride (PMSF).
625 The clarified cell lysate was incubated with Ni-NTA beads at 4°C for one hour, and the bound protein was
626 eluted with liner gradient of 20-500mM imidazole. The pooled fractions were buffer exchanged into 50
627 mM Tris, pH6.0, 20 mM NaCl, 2mM DTT. The sample was further purified using a HiTrap Q column (GE
628 Healthcare Life Sciences) followed by Superdex200 gel filtration chromatography (GE Healthcare Life
629 Sciences) and eluted in MOPS buffer. The protein was then concentrated, concentration quantified on a
630 nanospectrometer, aliquoted, and flash frozen in liquid nitrogen and stored in -80°C.

631 Single TPRs and J-domain were cloned using Gibson assembly into pMCSG7 plasmid. Protein
632 expression was induced that same as full-length DnaJC7 (see above). The TPR domains were purified
633 under denaturing conditions and refolded on Ni-NTA beads. Cell pellets were treated with 8M urea and
634 the lysate was centrifuged to remove debris. Denatured and clarified lysates were incubated with Ni-NTA
635 beads at 4°C for one hour. The Ni-NTA beads were washed with a decreasing gradient of urea using a
636 50 mM Tris pH 7.4, 500 mM NaCl, 1 mM β-mercaptoethanol base buffer. Finally, the beads were washed
637 with 50 mM Tris pH 7.4, 500 mM NaCl, 1 mM β-mercaptoethanol. Samples were eluted with 300mM
638 Imidazole in 50 mM Tris pH 7.4, 500 mM NaCl, 1 mM β-mercaptoethanol and applied to a superdex75
639 Increase 10/300 (GE) after concentration. Then samples were eluted in 30 mM MOPS pH7.4, 50 mM
640 KCl, 5mM MgCl₂ and 1 mM with DTT. The protein was then concentrated, concentration quantified on a
641 nanospectrometer, aliquoted, and flash frozen in liquid nitrogen and stored in -80°C.

642

643 **Microscale Thermophoresis**

644 MST experiments were performed on Nanotemper Monolith NT.115 in the Molecular Biophysics Resource
645 core at UTSW and analyzed with a standard protocol [62]. All binding measurements were done in

646 triplicates. Wild type or mutant Tau/K18 was labeled with Cyanine5 NHS ester dye (Cy5) and titrated by
647 a serial 2-fold dilution of DnaJC7 or single domain. For peptide binding, DnaJC7 was instead labeled with
648 Cy5. Data were fit in PALMIST in a 1:1 binding model and analyzed in GUSI [62].

649

650 **Cross-linking mass spectrometry analysis**

651 We have developed standardized protocols for crosslinking and data analysis of samples. For DSS
652 reactions, protein samples were cross-linked at 1mg/ml in 100 μ L total volume with a final 1mM DSS
653 (DSS-d₀ and -d₁₂, Creative Molecules) for three minutes at 37°C while shaking at 350rpm. For
654 ADH/DMTMM reactions, protein samples were incubated with 57mM ADH (d₀/d₈, Creative Molecules)
655 and 36mM DMTMM (Sigma-Aldrich) for 15 minutes at 37°C while shaking at 350 rpm. The reactions were
656 quenched with 100mM Ammonium Bicarbonate (AB) for 30 minutes. Samples were resolved on SDS-
657 PAGE gels (NUPAGE™, 4 to 12%, Bis-tris, 1.5mm or home-made SDS-Gel) and bands corresponding
658 to tauRD monomer, tau monomer, tauRD:DnaJC7 heterodimer or tau:DnaJC7 heterodimer were gel-
659 extracted following standard protocols [36]. Samples were flash frozen in liquid nitrogen, lyophilized and
660 resuspended in 8M urea followed by 2.5mM TCEP reduction and 5mM Iodoacetamide alkylation in dark
661 with each 30 minutes. Samples were then diluted to 1M urea by 50mM AB and digested by 1:50 (m/m)
662 trypsin (Promega) overnight shaking at 600rpm. 2% (v/v) formic acid was added to acidify the reaction
663 system and further purified by reverse-phase Sep-Pak tC18 cartridges (Waters) and size exclusion
664 peptide chromatography (SEPC). Fraction collected from SEPC was lyophilized. The dried samples were
665 resuspended in water/acetonitrile/formic acid (95:5:0.1, v/v/v) to a final concentration of approximately
666 0.5 μ g/ μ L. 2 μ L of each was injected into Eksigent 1D-NanoLC-Ultra HPLC system coupled to a Thermo
667 Orbitrap Fusion Tribrid system at the UTSW Proteomics core.

668

669 The analysis of the mass spectrum data was done by in-house version of xQuest [39]. Each Thermo.raw
670 data was first converted to open.mzXML format using msconvert (proteowizard.sourceforge.net). Search
671 parameters were set differently based on the cross-link reagent as followed. For DSS, maximum number
672 of missed cleavages (excluding the cross-linking site) = 2, peptide length = 5–50 aa, fixed
673 modifications = carbamidomethyl-Cys (mass shift = 57.021460 Da), mass shift of the light

674 crosslinker = 138.068080 Da, mass shift of mono-links = 156.078644 and 155.096428 Da,
675 MS1 tolerance = 10 ppm, MS2 tolerance = 0.2 Da for common ions and 0.3 Da for cross-link ions, search
676 in ion-tag mode. For zero-length crosslink search: maximum number of missed cleavages = 2, peptide
677 length = 5-50 residues, fixed modifications carbamidomethyl-Cys (mass shift = 57.02146 Da), mass shift
678 of crosslinker = -18.010595 Da, no monolink mass specified, MS1 tolerance = 15 ppm, and MS2 tolerance
679 = 0.2 Da for common ions and 0.3 Da for crosslink ions; search in enumeration mode. FDRs were
680 estimated by xprophet [63] to be 0% - 0.17%. For each experiment, five replicate data sets were
681 compared and only crosslink pairs appeared at least in three data sets were used to generate a
682 consensus data (Supplementary Table 2). The pairs position and unique nseen numbers (frequency)
683 were visualized using custom gunplot script.

684

685 **¹⁵N-¹H TROSY-HSQC**

686 Two-dimensional ¹⁵N-¹H TROSY-HSQC spectra were recorded on Agilent DD2 600MHZ spectrometers
687 at the UT Southwestern Biomolecular NMR Facility. The ¹⁵N labeled K18 and DnaJC7 were both buffer
688 exchanged into 10mM Na₂HPO₄ pH 7.4, 100 mM NaCl, 4mM DTT with 8% D₂O. Each HSQC run was
689 performed at 10°C with either ¹⁵N labeled K18 alone or titrated by DnaJC7 with molar ratio at 1:0.5, 1:1,
690 1:2. Spectrum was converted phase corrected using NMRPipe [64]. Peak assignments were based on
691 the deposited information from BMRB (19253) and unpublished data from Dr. Guy Lippens. The
692 software Sparky was used to analyze chemical shift perturbations across concentrations [65].

693

694 **Thioflavin (ThT) aggregation assay**

695 Wild-type or mutated full-length and tauRD (i.e. K18) was diluted to 17.6 μM in MOPS buffer with 25 uM
696 β-mercaptoethanol and boiled at 100°C for 5 min. A further two-fold dilution in PBS was followed and a
697 final concentration of 25 μM ThT was added in dark. For a 60 μL reaction system, 30 μL tau or RD protein
698 was mixed with equal volume of a mixture consisting of either buffer, seeding monomer, DnaJC7, tauRD,
699 tau, WT R1R2 or P270S R1R2 or any combination of them [36]. All experiments were performed in
700 triplicate. ThT kinetic scans were run every 10 min on a Tecan Spark plate reader at 446 nm Ex (5 nm
701 bandwidth), 482 nm Em (5 nm bandwidth) with agitation for 5s prior to acquisition.

702

703 **Transmission Electron Microscopy**

704 An aliquot of 5 μ L sample was loaded onto a glow-discharged Formvar-coated 200-mesh copper grids
705 for 30 s and was blotted by filter paper followed by washing the grid with 5 μ L ddH₂O. After another 30
706 seconds, 2% uranyl acetate was loaded on the grids and blotted again. The grid was dried for 1min and
707 loaded into a FEI Tecnai G2 Spirit Biotwin TEM. All images were captured using a Gatan 2Kx2K multiport
708 readout post column CCD at the UT Southwestern EM Core Facility.

709

710 **Modeling tau and its interaction with DnaJC7**

711 Modeling of the tau repeat domain was performed using CS-ROSETTA guided by backbone chemical
712 shifts kindly provided by Guy Lippens. 5000 models of tau repeat domain were produced on the biohpc
713 cluster. Chemical shift perturbations were mapped onto a representative model using an in-house python
714 script. R1R2 or R2R3 sequence elements were extracted from the 5000-model ensemble and the
715 conformations were structurally aligned to produce a small set of unique conformation using the cluster
716 protocol in Rosetta. Models of DnaJC7 were built homology modeling by employing a DnaJC5 structural
717 model as a template. The resulting models were relaxed and the lowest scoring models were selected
718 for subsequent analysis [40]. The EnsembleDock protocol [66] allowed the docking of an ensemble of
719 R1R2 and R2R3 peptide conformations (from above) against an ensemble of DnaJC7 conformations
720 using first a low-resolution centroid mode, followed by full-atom relax. The change in binding energy was
721 calculated using the ddg protocol to evaluate the predicted binding energy [28]. Additionally, for each
722 model in the ensemble we computed the distance between C α -C α atoms between tau:DnaJC7 for
723 positions that crosslinked in the XLMS experiments using an in-house python script [36]. The predicted
724 binding energy was plotted as a function of the crosslink distance geometry to identify models with low
725 energy that satisfied our experimental data. All simulations were performed on UTSW's biohpc computing
726 cluster. All plots were generated with gnuplot. Images were created using Pymol.

727

728 References

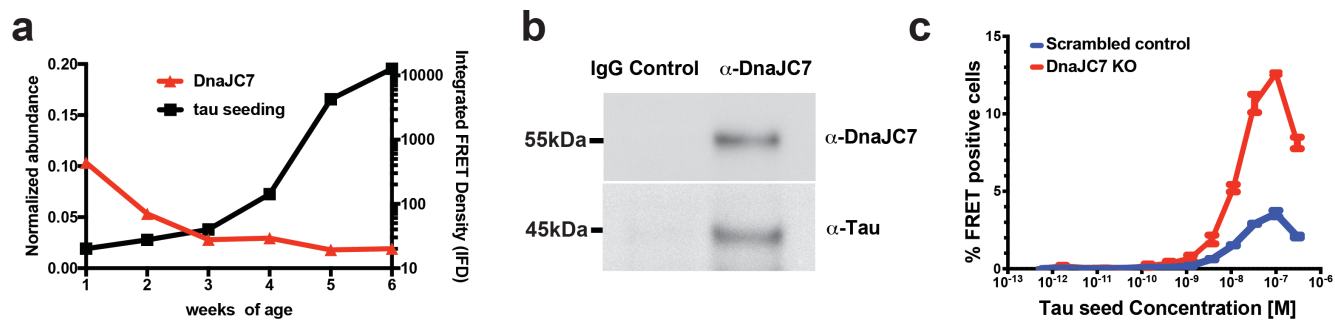
729

- 730 1. Mayer, M.P. and B. Bukau, *Hsp70 chaperones: cellular functions and molecular mechanism*.
731 Cell Mol Life Sci, 2005. **62**(6): p. 670-84.
- 732 2. Witt, S.N., *Hsp70 molecular chaperones and Parkinson's disease*. Biopolymers, 2010. **93**(3): p.
733 218-28.
- 734 3. Turturici, G., G. Sconzo, and F. Geraci, *Hsp70 and its molecular role in nervous system*
735 *diseases*. Biochem Res Int, 2011. **2011**: p. 618127.
- 736 4. Klucken, J., et al., *Hsp70 Reduces alpha-Synuclein Aggregation and Toxicity*. J Biol Chem,
737 2004. **279**(24): p. 25497-502.
- 738 5. Takeuchi, H., et al., *Hsp70 and Hsp40 improve neurite outgrowth and suppress intracytoplasmic*
739 *aggregate formation in cultured neuronal cells expressing mutant SOD1*. Brain Res, 2002.
740 **949**(1-2): p. 11-22.
- 741 6. Kobayashi, Y. and G. Sobue, *Protective effect of chaperones on polyglutamine diseases*. Brain
742 Res Bull, 2001. **56**(3-4): p. 165-8.
- 743 7. Jinwal, U.K., et al., *Imbalance of Hsp70 family variants fosters tau accumulation*. FASEB J,
744 2013. **27**(4): p. 1450-9.
- 745 8. Lu, R.C., et al., *Heat shock protein 70 in Alzheimer's disease*. Biomed Res Int, 2014. **2014**: p.
746 435203.
- 747 9. Kityk, R., J. Kopp, and M.P. Mayer, *Molecular Mechanism of J-Domain-Triggered ATP*
748 *Hydrolysis by Hsp70 Chaperones*. Mol Cell, 2018. **69**(2): p. 227-237 e4.
- 749 10. Kampinga, H.H. and E.A. Craig, *The HSP70 chaperone machinery: J proteins as drivers of*
750 *functional specificity*. Nat Rev Mol Cell Biol, 2010. **11**(8): p. 579-92.
- 751 11. Tiwari, S., et al., *Unique structural modulation of a non-native substrate by cochaperone DnaJ*.
752 Biochemistry, 2013. **52**(6): p. 1011-8.
- 753 12. Hageman, J. and H.H. Kampinga, *Computational analysis of the human HSPH/HSPA/DNAJ*
754 *family and cloning of a human HSPH/HSPA/DNAJ expression library*. Cell Stress Chaperones,
755 2009. **14**(1): p. 1-21.
- 756 13. Cajo, G.C., et al., *The role of the DIF motif of the DnaJ (Hsp40) co-chaperone in the regulation*
757 *of the DnaK (Hsp70) chaperone cycle*. J Biol Chem, 2006. **281**(18): p. 12436-44.
- 758 14. Hartl, F.U., *Molecular chaperones in cellular protein folding*. Nature, 1996. **381**(6583): p. 571-9.
- 759 15. Kampinga, H.H., et al., *Function, evolution, and structure of J-domain proteins*. Cell Stress
760 Chaperones, 2019. **24**(1): p. 7-15.
- 761 16. Blair, L.J., J.J. Sabbagh, and C.A. Dickey, *Targeting Hsp90 and its co-chaperones to treat*
762 *Alzheimer's disease*. Expert Opin Ther Targets, 2014. **18**(10): p. 1219-32.
- 763 17. Farhan, S.M.K., et al., *Exome sequencing in amyotrophic lateral sclerosis implicates a novel*
764 *gene, DNAJC7, encoding a heat-shock protein*. Nat Neurosci, 2019. **22**(12): p. 1966-1974.
- 765 18. Brychzy, A., et al., *Cofactor Tpr2 combines two TPR domains and a J domain to regulate the*
766 *Hsp70/Hsp90 chaperone system*. EMBO J, 2003. **22**(14): p. 3613-23.
- 767 19. Schulke, J.P., et al., *Differential impact of tetratricopeptide repeat proteins on the steroid*
768 *hormone receptors*. PLoS One, 2010. **5**(7): p. e11717.
- 769 20. Ohno, M., et al., *The roles of co-chaperone CCRP/DNAJC7 in Cyp2b10 gene activation and*
770 *steatosis development in mouse livers*. PLoS One, 2014. **9**(12): p. e115663.
- 771 21. Graham, J.B., N.P. Canniff, and D.N. Hebert, *TPR-containing proteins control protein*
772 *organization and homeostasis for the endoplasmic reticulum*. Crit Rev Biochem Mol Biol, 2019.
773 **54**(2): p. 103-118.
- 774 22. Alvira, S., et al., *Structural characterization of the substrate transfer mechanism in Hsp70/Hsp90*
775 *folding machinery mediated by Hop*. Nat Commun, 2014. **5**: p. 5484.
- 776 23. Kim, Y.E., et al., *Soluble Oligomers of PolyQ-Expanded Huntingtin Target a Multiplicity of Key*
777 *Cellular Factors*. Mol Cell, 2016. **63**(6): p. 951-64.
- 778 24. Sui, X.J., et al., *Widespread remodeling of proteome solubility in response to different protein*
779 *homeostasis stresses*. Proceedings of the National Academy of Sciences of the United States of
780 America, 2020. **117**(5): p. 2422-2431.
- 781 25. Kolarova, M., et al., *Structure and pathology of tau protein in Alzheimer disease*. Int J
782 Alzheimers Dis, 2012. **2012**: p. 731526.
- 783 26. Falcon, B., et al., *Conformation determines the seeding potencies of native and recombinant*
784 *Tau aggregates*. J Biol Chem, 2015. **290**(2): p. 1049-65.

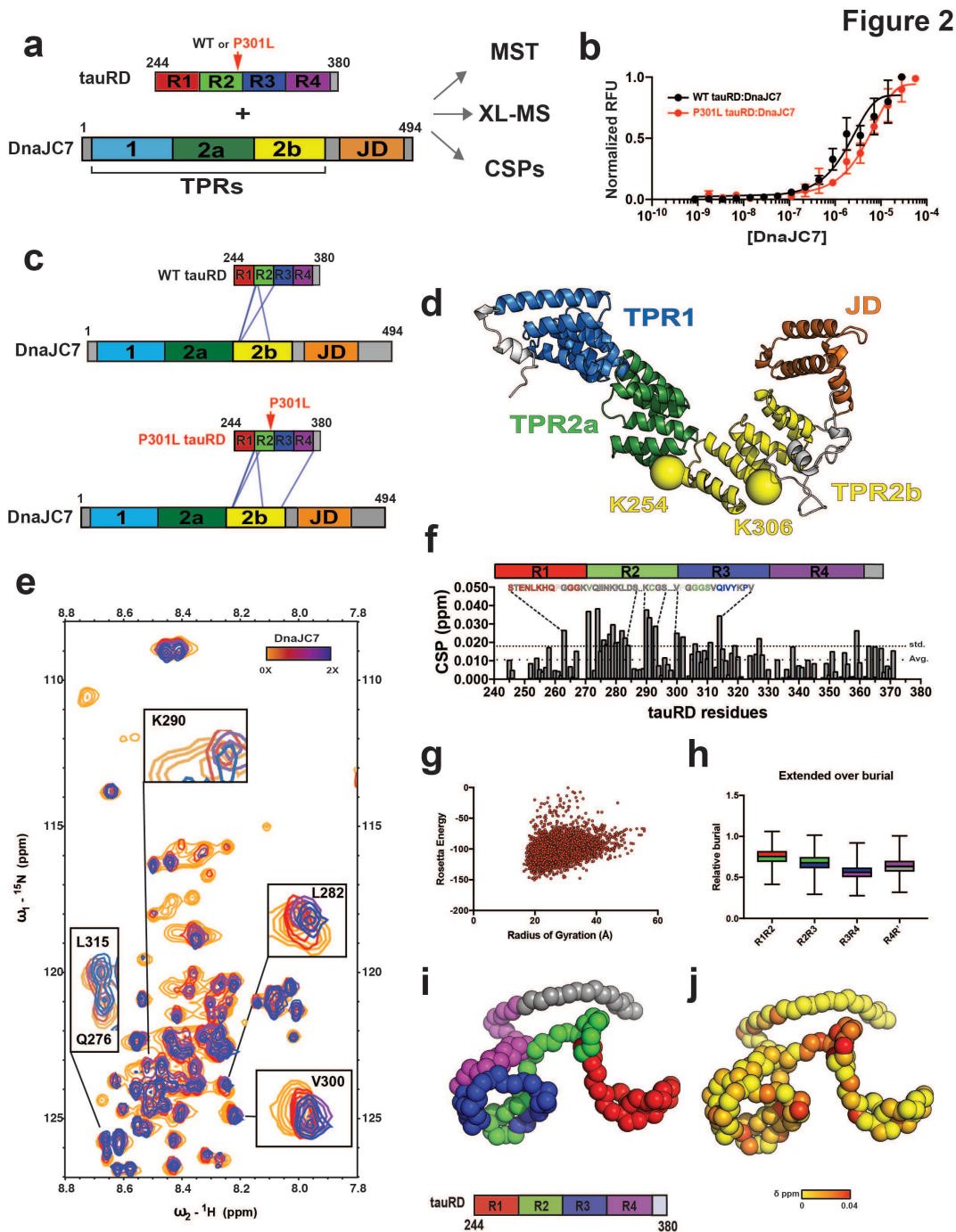
- 785 27. Combs, B., C. Hamel, and N.M. Kanaan, *Pathological conformations involving the amino*
786 *terminus of tau occur early in Alzheimer's disease and are differentially detected by monoclonal*
787 *antibodies*. Neurobiol Dis, 2016. **94**: p. 18-31.
- 788 28. Mirbaha, H., et al., *Inert and seed-competent tau monomers suggest structural origins of*
789 *aggregation*. Elife, 2018. **7**.
- 790 29. Holmes, B.B., et al., *Proteopathic tau seeding predicts tauopathy in vivo*. Proc Natl Acad Sci U
791 S A, 2014. **111**(41): p. E4376-85.
- 792 30. Nachman, E., et al., *Disassembly of Tau fibrils by the human Hsp70 disaggregation machinery*
793 *generates small seeding-competent species*. J Biol Chem, 2020. **295**(28): p. 9676-9690.
- 794 31. Mok, S.A., et al., *Mapping interactions with the chaperone network reveals factors that protect*
795 *against tau aggregation*. Nat Struct Mol Biol, 2018. **25**(5): p. 384-393.
- 796 32. Aprile, F.A., et al., *The molecular chaperones DNAJB6 and Hsp70 cooperate to suppress alpha-*
797 *synuclein aggregation*. Sci Rep, 2017. **7**(1): p. 9039.
- 798 33. Iba, M., et al., *Synthetic tau fibrils mediate transmission of neurofibrillary tangles in a transgenic*
799 *mouse model of Alzheimer's-like tauopathy*. J Neurosci, 2013. **33**(3): p. 1024-37.
- 800 34. Doench, J.G., et al., *Optimized sgRNA design to maximize activity and minimize off-target*
801 *effects of CRISPR-Cas9*. Nat Biotechnol, 2016. **34**(2): p. 184-191.
- 802 35. Li, W. and V.M. Lee, *Characterization of two VQIXXK motifs for tau fibrillization in vitro*.
803 Biochemistry, 2006. **45**(51): p. 15692-701.
- 804 36. Chen, D., et al., *Tau local structure shields an amyloid-forming motif and controls aggregation*
805 *propensity*. Nat Commun, 2019. **10**(1): p. 2493.
- 806 37. Yu, A., et al., *Tau protein aggregates inhibit the protein-folding and vesicular trafficking arms of*
807 *the cellular proteostasis network*. J Biol Chem, 2019. **294**(19): p. 7917-7930.
- 808 38. Leitner, A., et al., *Crosslinking and Mass Spectrometry: An Integrated Technology to*
809 *Understand the Structure and Function of Molecular Machines*. Trends Biochem Sci, 2016.
810 **41**(1): p. 20-32.
- 811 39. Rinner, O., et al., *Identification of cross-linked peptides from large sequence databases*. Nat
812 Methods, 2008. **5**(4): p. 315-8.
- 813 40. Simons, K.T., et al., *Ab initio protein structure prediction of CASP III targets using ROSETTA*.
814 Proteins, 1999. **Suppl 3**: p. 171-6.
- 815 41. Barre, P. and D. Eliezer, *Structural transitions in tau k18 on micelle binding suggest a hierarchy*
816 *in the efficacy of individual microtubule-binding repeats in filament nucleation*. Protein Sci, 2013.
817 **22**(8): p. 1037-48.
- 818 42. Nerli, S. and N.G. Sgourakis, *Cs-Rosetta*. Methods Enzymol, 2019. **614**: p. 321-362.
- 819 43. Novak, P., et al., *Tau Conformation as a Target for Disease-Modifying Therapy: The Role of*
820 *Truncation*. J Alzheimers Dis, 2018. **64**(s1): p. S535-S546.
- 821 44. Zabik, N.L., M.M. Imhof, and S. Martic-Milne, *Structural evaluations of tau protein conformation:*
822 *methodologies and approaches*. Biochem Cell Biol, 2017. **95**(3): p. 338-349.
- 823 45. Falcon, B., et al., *Novel tau filament fold in chronic traumatic encephalopathy encloses*
824 *hydrophobic molecules*. Nature, 2019. **568**(7752): p. 420-423.
- 825 46. Fitzpatrick, A.W.P., et al., *Cryo-EM structures of tau filaments from Alzheimer's disease*. Nature,
826 2017. **547**(7662): p. 185-190.
- 827 47. Zhang, W., et al., *Novel tau filament fold in corticobasal degeneration*. Nature, 2020. **580**(7802):
828 p. 283-287.
- 829 48. Falcon, B., et al., *Structures of filaments from Pick's disease reveal a novel tau protein fold*.
830 Nature, 2018. **561**(7721): p. 137-140.
- 831 49. Baaklini, I., et al., *Selective Binding of HSC70 and its Co-Chaperones to Structural Hotspots on*
832 *CFTR*. Sci Rep, 2020. **10**(1): p. 4176.
- 833 50. Rudiger, S., J. Schneider-Mergener, and B. Bukau, *Its substrate specificity characterizes the*
834 *DnaJ co-chaperone as a scanning factor for the DnaK chaperone*. EMBO J, 2001. **20**(5): p.
835 1042-50.
- 836 51. Freilich, R., et al., *Competing protein-protein interactions regulate binding of Hsp27 to its client*
837 *protein tau*. Nat Commun, 2018. **9**(1): p. 4563.
- 838 52. Young, Z.T., et al., *Stabilizing the Hsp70-Tau Complex Promotes Turnover in Models of*
839 *Tauopathy*. Cell Chem Biol, 2016. **23**(8): p. 992-1001.

- 840 53. Ramsey, A.J., L.C. Russell, and M. Chinkers, *C-terminal sequences of hsp70 and hsp90 as*
841 *non-specific anchors for tetratricopeptide repeat (TPR) proteins*. *Biochem J*, 2009. **423**(3): p.
842 411-9.
- 843 54. Muller, P., et al., *C-terminal phosphorylation of Hsp70 and Hsp90 regulates alternate binding to*
844 *co-chaperones CHIP and HOP to determine cellular protein folding/degradation balances*.
845 *Oncogene*, 2013. **32**(25): p. 3101-10.
- 846 55. Johnson, B.D., et al., *Hop modulates Hsp70/Hsp90 interactions in protein folding*. *J Biol Chem*,
847 1998. **273**(6): p. 3679-86.
- 848 56. Assimon, V.A., D.R. Southworth, and J.E. Gestwicki, *Specific Binding of Tetratricopeptide*
849 *Repeat Proteins to Heat Shock Protein 70 (Hsp70) and Heat Shock Protein 90 (Hsp90) Is*
850 *Regulated by Affinity and Phosphorylation*. *Biochemistry*, 2015. **54**(48): p. 7120-7131.
- 851 57. Karagoz, G.E., et al., *Hsp90-Tau complex reveals molecular basis for specificity in chaperone*
852 *action*. *Cell*, 2014. **156**(5): p. 963-74.
- 853 58. Kundel, F., et al., *Hsp70 Inhibits the Nucleation and Elongation of Tau and Sequesters Tau*
854 *Aggregates with High Affinity*. *ACS Chem Biol*, 2018. **13**(3): p. 636-646.
- 855 59. Sanson, K.R., et al., *Optimized libraries for CRISPR-Cas9 genetic screens with multiple*
856 *modalities*. *Nat Commun*, 2018. **9**(1): p. 5416.
- 857 60. Sanjana, N.E., O. Shalem, and F. Zhang, *Improved vectors and genome-wide libraries for*
858 *CRISPR screening*. *Nat Methods*, 2014. **11**(8): p. 783-784.
- 859 61. Stopschinski, B.E., et al., *Specific glycosaminoglycan chain length and sulfation patterns are*
860 *required for cell uptake of tau versus alpha-synuclein and beta-amyloid aggregates*. *J Biol*
861 *Chem*, 2018. **293**(27): p. 10826-10840.
- 862 62. Scheuermann, T.H., et al., *On the acquisition and analysis of microscale thermophoresis data*.
863 *Anal Biochem*, 2016. **496**: p. 79-93.
- 864 63. Walzthoeni, T., et al., *False discovery rate estimation for cross-linked peptides identified by*
865 *mass spectrometry*. *Nat Methods*, 2012. **9**(9): p. 901-3.
- 866 64. Delaglio, F., et al., *NMRPipe: a multidimensional spectral processing system based on UNIX*
867 *pipes*. *J Biomol NMR*, 1995. **6**(3): p. 277-93.
- 868 65. Lee, W., M. Tonelli, and J.L. Markley, *NMRFAM-SPARKY: enhanced software for biomolecular*
869 *NMR spectroscopy*. *Bioinformatics*, 2015. **31**(8): p. 1325-7.
- 870 66. Schueler-Furman, O., C. Wang, and D. Baker, *Progress in protein-protein docking: atomic*
871 *resolution predictions in the CAPRI experiment using RosettaDock with an improved treatment*
872 *of side-chain flexibility*. *Proteins*, 2005. **60**(2): p. 187-94.
- 873
874
875
876
877
878
879
880
881
882
883
884
885
886
887
888
889
890
891
892
893
894

Figure 1



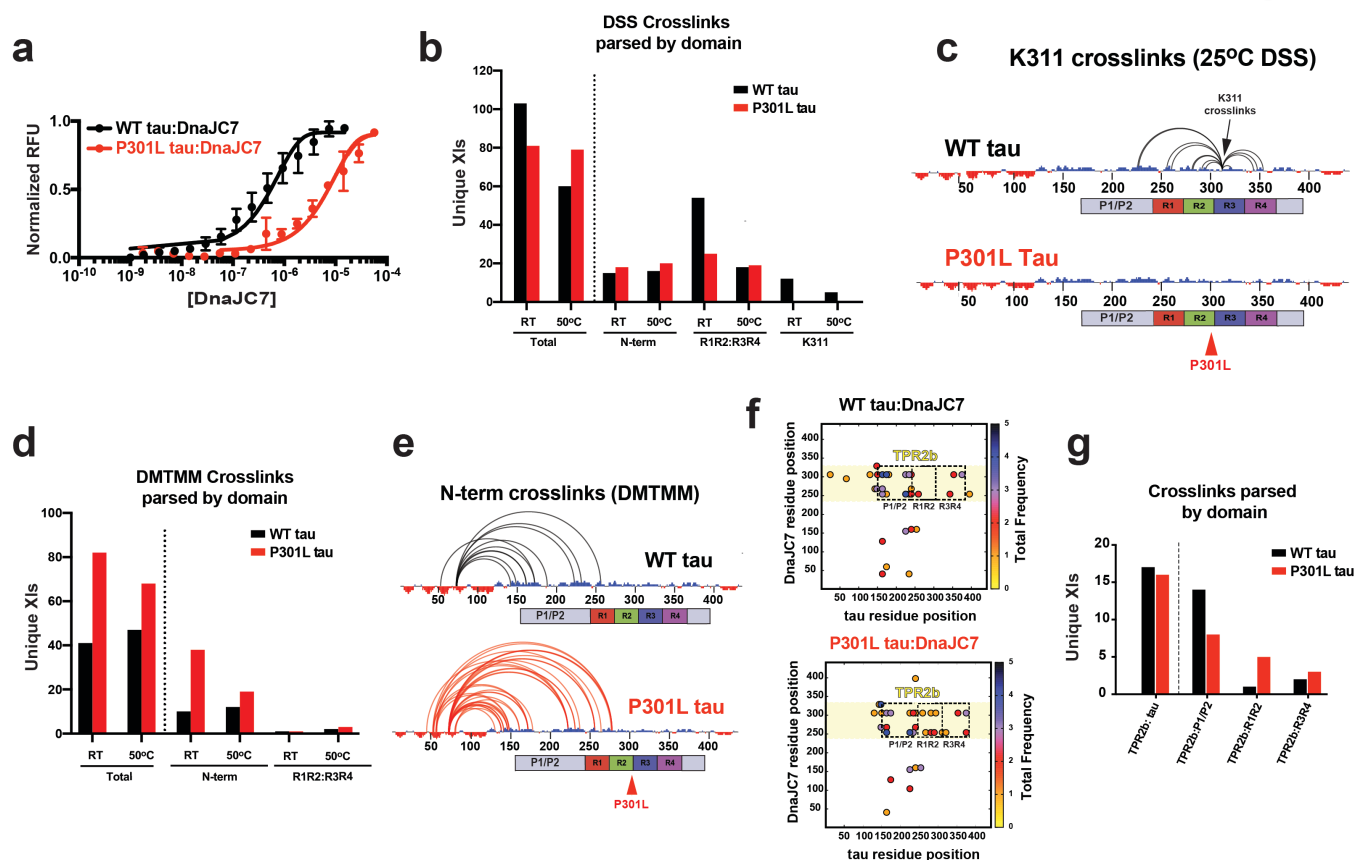
897
898
899 **Figure 1. Identification of a novel Hsp40 DnaJC7 that binds to tau and influences seeding.**
900 **a.** Immunoprecipitation of tau from PS19 tauopathy mice across different ages (weeks 1 through
901 5) reveals an increase in seeding activity at early ages (black) which anti-correlates with a 5-fold
902 decrease of Hsp40 DnaJC7 abundance (red). Isolated tau from the different samples were
903 evaluated for the presence of pathogenic seeds using tau biosensors (right y-axis) and the
904 normalized abundance of DnaJC7 (relative to P301S 1N4R tau; $[I_{\text{Hsp40}}/I_{\text{tau}}] \times 100$) was determined
905 using mass spectrometry (left y-axis). Seeding experiments were performed in triplicate and the
906 mass spectrometry data were analyzed using Proteome Discoverer (Thermo). **b.** Co-
907 immunoprecipitation of DnaJC7 and tau from PS19 mouse brain lysates. Brain lysates were
908 immunoprecipitated with an anti-DnaJC7 antibody or an IgG antibody as negative control. The
909 immunoprecipitates were analyzed by Western blot analysis and probed with anti-DnaJC7 or
910 anti-tau antibodies. **c.** Dose titration of recombinant heparin-induced tau fibril seeding on the
911 tauRD mClover3/mCerulean biosensor cells. Cells were treated with tau fibril concentrations
912 performed as three-fold dilutions ranging from 300 nM down to 565 fM. Seeding was quantified
913 via flow cytometry based on the percentage of FRET-positive cells in each sample. The decrease
914 in seeding at 300 nM corresponds to cell death due to toxicity of high concentrations of tau fibrils.
915 Seeding experiments were performed in triplicate and are shown as averages with standard
916 deviation.
917



918
 919 **Figure 2. DnaJC7 binds directly to tauRD through the R1R2 inter-repeat element.**
 920 **a.** Schematic representation of the DnaJC7 and tauRD constructs used to probe their interaction.
 921 TauRD domains are colored in red, green, blue and magenta for repeats 1, 2, 3 and 4,
 922 respectively. DnaJC7 domains are colored in light blue, dark green, yellow and orange for TPR1,
 923 TPR2a, TPR2b and J-domain, respectively. **b.** MST assay to quantify affinity between tauRD
 924 (WT and P301L) and DnaJC7. The tauRD:DnaJC7 and P301L tauRD:DnaJC7 binding curves
 925 are colored in black and red, respectively. The MST binding experiments were performed in
 926 triplicate and each concentration point is shown as an average with standard deviation. The data
 927 were fit to a linear regression model to estimate the binding constant. **c.** XL-MS to identify the
 928 interactions in the complex. Each protein is shown as cartoon schematic and the crosslinks are
 929 shown as blue lines linking the two crosslinked positions. The constructs are colored as in (a).
 930 **d.** DnaJC7 homology model shown in cartoon representation and the domains are in

931 (a). The two major crosslink sites in TPR2b are shown as spheres and colored by the domain.
932 e. 2D ^1H - ^{15}N HSQC spectra of tauRD in the absence (red) and in the presence of increasing
933 DnaJC7 concentrations. Molar ratio of tauRD to DnaJC7 is 2:1 (yellow), 1:1 (red), 1:2 (blue). Key
934 peaks that are significantly perturbed in the presence of DnaJC7 are shown as insets and labeled
935 by the amino acid position. f. NMR CSPs of tauRD in 1:1 molar ratio of DnaJC7 are shown as a
936 bar plot colored in grey. The amino acid residues for tauRD that are significantly shifted are
937 shown above the bar plot, the remaining residues are colored as in (a). The tauRD cartoon is
938 shown above the plot and the domains are colored as in (a). Residues that are significantly
939 perturbed are consistent with the region identified by XL-MS. Average and standard deviations
940 are shown as dashed lines. g. Left panel, Rosetta Energy and calculated radius of gyration is
941 shown for an ensemble of tauRD models built by CS-ROSETTA. h. Ensemble average of
942 normalized solvent exposure (normalized to solvent exposure of a fully extended chain) for inter-
943 repeat elements R1R2, R2R3, R3R4 and R4R' is shown as a box plot and colored red/green,
944 green/blue, blue/magenta and magenta/grey, respectively. Consistent with DnaJC7 the R1R2
945 element appears most exposed. i. Representative model of tau RD from the ensemble highlights
946 relative exposure of the R1R2 element. The backbone of the model is shown in spacefill and is
947 colored as in (a). j. The backbone of the model is shown in spacefill and shown in the same
948 orientation as (i). tauRD model is colored according to DnaJC7-induced CSPs color-coded from
949 yellow (0 ppm) to red (0.04 ppm).

950
951
952
953
954
955
956
957
958
959
960
961
962
963
964
965
966
967
968
969
970
971
972
973

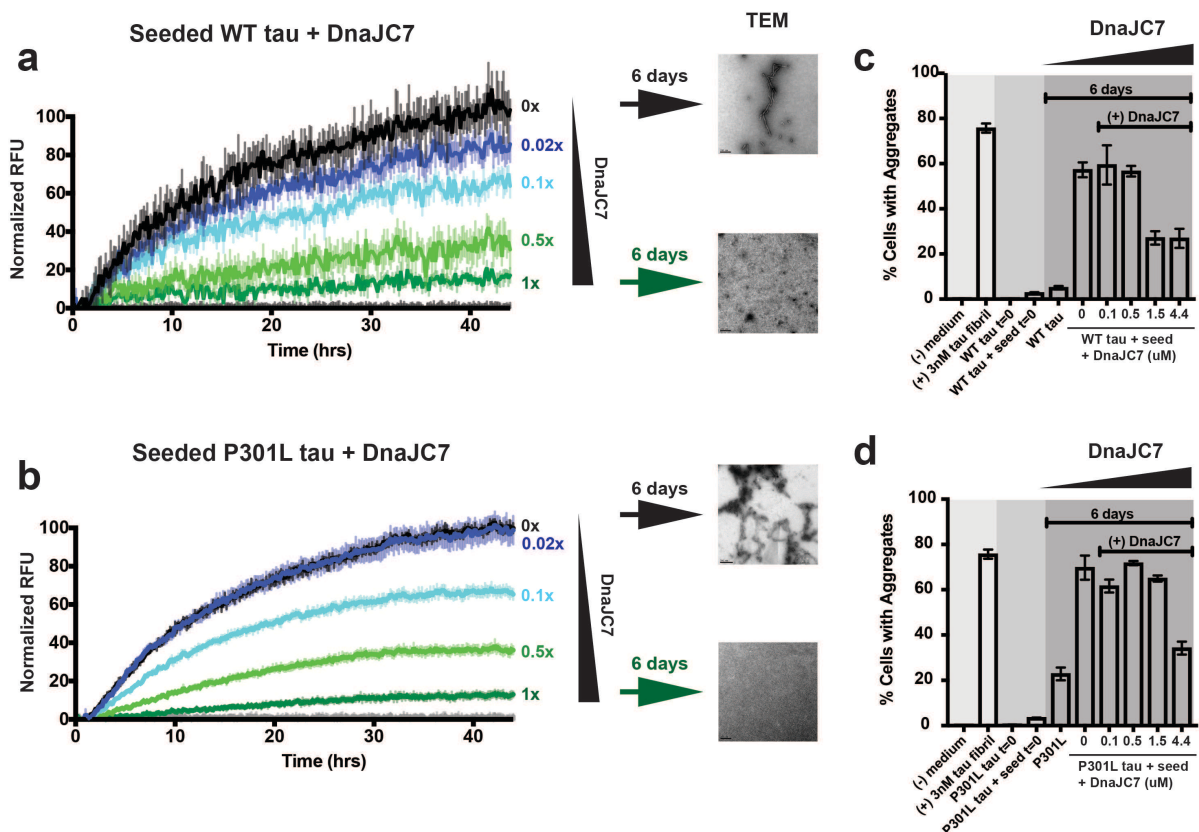


974
 975 **Figure 3. Pathogenic P301L mutation alters tau dynamics and impacts DnaJC7 binding**
 976 **affinity.** **a.** MST to quantify affinity of full-length tau (WT/P301L) and DnaJC7. The WT
 977 tau:DnaJC7 and P301L tau:DnaJC7 binding curves are colored in black and red, respectively.
 978 The MST binding experiments were performed in triplicate and are shown as an average with
 979 standard deviation. The data were fit to a linear regression model to estimate the binding
 980 constant. **b.** Unique consensus DSS crosslink pairs identified in WT and P301L tau are shown
 981 as a bar plot comparing total crosslinks and crosslinks parsed by different domains (N-terminus,
 982 R1R2:R3R4 and K311) and acquired at RT and 50°C. Changes in the distribution of crosslinks
 983 across the domains in tau highlight differences in conformation. WT tau and P301L tau crosslinks
 984 are colored in black and red, respectively. **c.** Consensus crosslinks involving K311 are shown
 985 for WT and P301L tau. The P301L mutation abolishes crosslinks to K311 disfavoring the local
 986 compact structure as measured by the absence of crosslinks at K311 in proximity to the
 987 mutation. The crosslinks are shown as semi-circles mapped onto the linear sequence of tau.
 988 The net charge per residue (NCPR) distribution is shown on the sequence axis to highlight
 989 regions with predominantly acidic (red) or basic (blue) sequence elements. Cartoon domain for
 990 tau is shown below the sequence axis, the domains are colored as in Fig. 2a. **d.** Unique
 991 consensus DMTMM crosslink pairs identified in WT and P301L tau are shown as a bar plot
 992 comparing total crosslinks and crosslinks parsed by different domains (N-terminus and
 993 R1R2:R3R4) and acquired at RT and 50°C. Changes in the distribution of crosslinks across the
 994 domains in tau highlight differences in the conformation of the N-terminal contacts. WT tau and
 995 P301L tau crosslinks are colored in black and red, respectively. **e.** Consensus crosslinks
 996 between the acidic N-terminus and the basic regions of tau (mostly repeat domain). The P301L
 997 mutation dramatically increases the heterogeneity of acidic-basic contacts from the N-terminus
 998 to the repeat domain compared to WT tau. The crosslinks are shown as semi-circles mapped
 999 onto the linear sequence of tau and are colored black and red for WT and P301L tau,
 1000 respectively. NCPR distribution is shown on the sequence axis to highlight regions with

1001 predominantly acidic (red) or basic (blue) sequence elements. Cartoon domain for tau is shown
1002 below the sequence axis, the domains are colored as in Fig. 2a. **f.** Consensus WT tau:DnaJC7
1003 (top) and P301L tau:DnaJC7 (bottom) inter-molecular DSS crosslink contact map colored by
1004 average frequency across replicates. TPR2b dominates the contacts with tau but the contacts
1005 are differentially redistributed across P1/P2 and R1R2 for WT tau and P301L tau. **g.** Unique
1006 consensus DSS crosslink pairs identified in WT tau:DnaJC7 and P301L tau:DnaJC7 are shown
1007 as a bar plot comparing total crosslinks and crosslinks parsed by DnaJC7 TPR2b contacts to
1008 different regions on tau (N-terminus, R1R2 and R3R4). In WT tau, tighter binding to DNAJC7
1009 buries R1R2 and exposes P1P2 domain, hence, leading to decreased crosslinks in R1R2 and
1010 increased crosslinks in P1P2. WT tau and P301L tau crosslinks are colored in black and red,
1011 respectively.

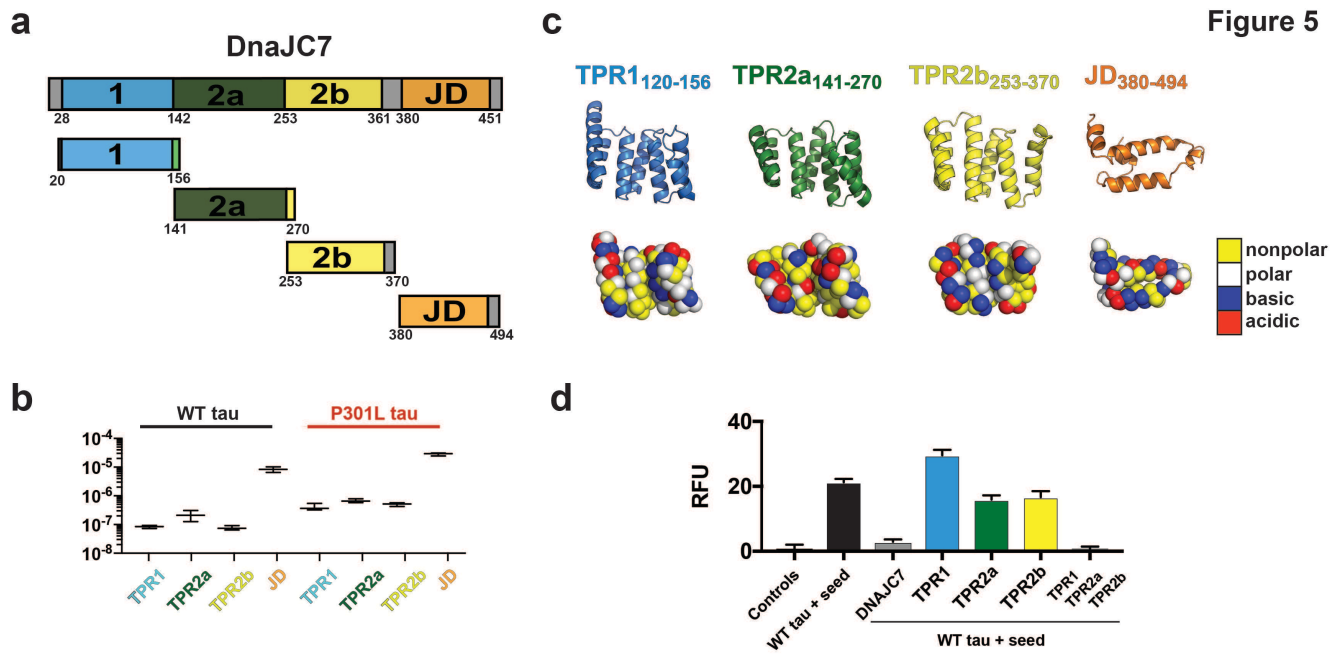
1012
1013
1014
1015
1016
1017
1018
1019
1020
1021
1022
1023
1024
1025
1026
1027
1028
1029
1030
1031
1032
1033
1034
1035
1036
1037
1038
1039
1040
1041
1042
1043
1044

Figure 4



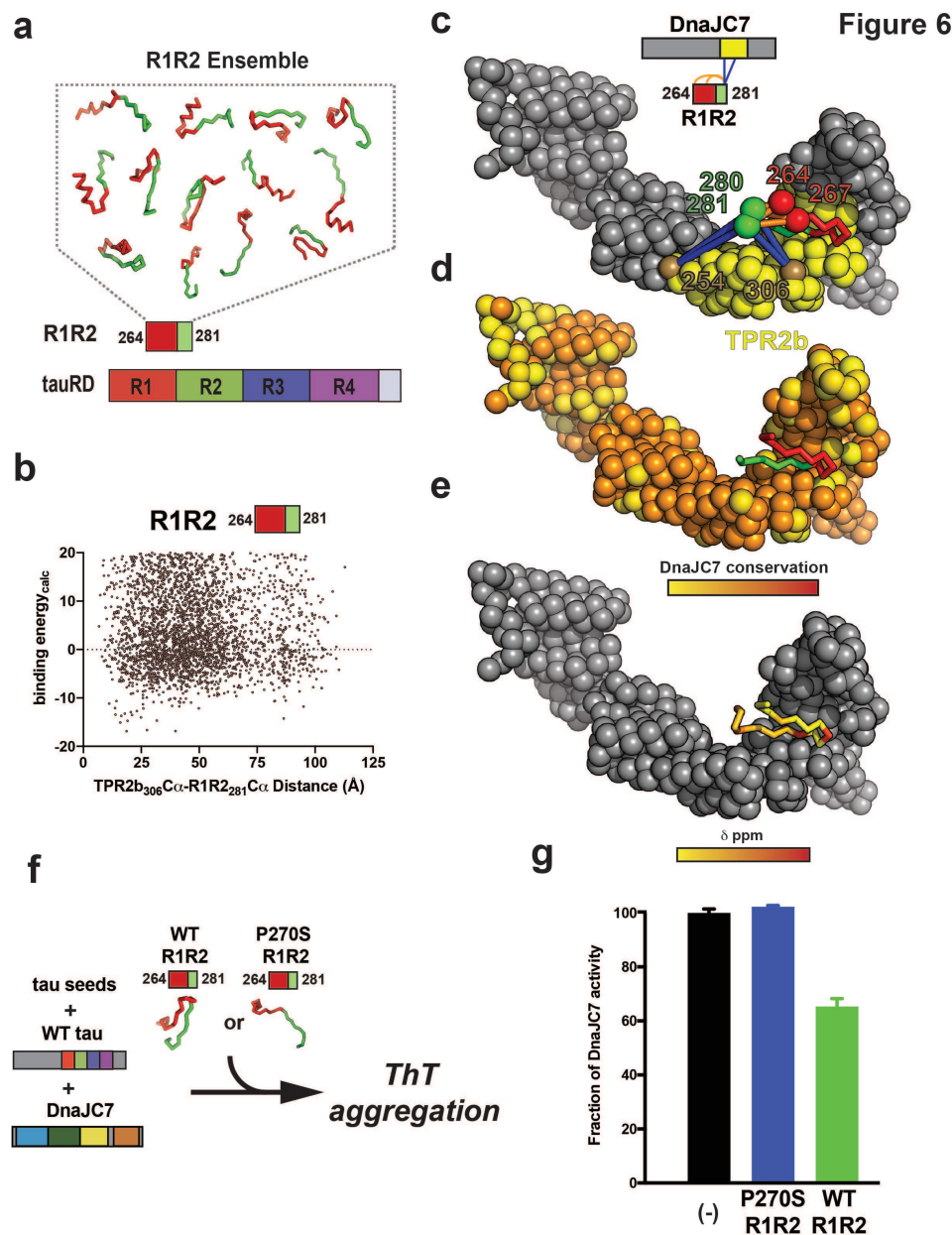
1045
 1046 **Figure 4. DnaJC7 efficiently suppresses tau aggregation *in vitro*.** 4.4 μ M WT tau (a) and
 1047 4.4 μ M P301L tau (b) aggregation was induced using 50nM tau monomer seeds in the presence
 1048 of different DnaJC7 chaperone concentrations. Aggregation was monitored using ThT
 1049 fluorescence. Experiments were performed in triplicate and are shown as averages with
 1050 standard deviation. DnaJC7 concentrations ranged from 0X (0uM), 0.02X (0.1uM), 0.1X
 1051 (0.5uM), 0.35X (1.5uM), to 1X (4.4uM) and are colored from black to green. Grey curves show
 1052 negative controls: tau alone, DnaJC7 alone at each concentration and tau monomer seeds
 1053 alone. TEM images were taken at the end point to confirm the presence or absence of fibrils. (c-
 1054 d) The endpoint and control samples of the *in vitro* aggregation experiment were assayed for
 1055 seeding activity in tau biosensors cells. The in-cell aggregation assay shows significant reduction
 1056 in seeding in the presence of DnaJC7 even after 6 days of incubation and is consistent with the
 1057 *in vitro* measurements. Tau seeding experiments were performed in triplicate and are shown as
 1058 averages with standard deviation.

1059
 1060
 1061
 1062
 1063
 1064
 1065
 1066
 1067
 1068
 1069
 1070



1072
 1073
 1074 **Figure 5. Efficient DnaJC7 suppression of tau aggregation relies on all three TPR**
 1075 **domains.** **a.** Schematic diagram of DnaJC7 domain constructs used: TPR₁₂₀₋₁₅₆ (light blue),
 1076 TPR2a₁₄₁₋₂₇₀ (dark green), TPR2b₂₅₃₋₃₇₀ (yellow) and JD₃₈₀₋₄₉₄ (orange). **b.** MST binding affinity
 1077 summary of TPR construct WT tau and P301L tau. Binding experiments were performed in
 1078 triplicate and fitted to linear regression curve to estimate binding constants. The derived binding
 1079 constants are shown as averages with standard deviations across replicate experiments. WT
 1080 tau and P301L tau binding experiments are shown in black and red, respectively and the TPR
 1081 labels are colored according to the TPR domain as in (a). **c.** Cartoon representation of TPR₁₂₀₋
 1082 ₁₅₆ (light blue), TPR2a₁₄₁₋₂₇₀ (dark green), TPR2b₂₅₃₋₃₇₀ (yellow) and JD₃₈₀₋₄₉₄ (orange) oriented to
 1083 highlight the peptide binding groove. Spacefill representation of each domain is colored
 1084 according to amino acid properties; polar (white), nonpolar (yellow), acidic (red) and basic (blue)
 1085 residues. **d.** Individual TPR domains were used in a ThT Fluorescence aggregation assay to
 1086 measure their effect on suppressing tau aggregation *in vitro*. The end point of each experiment
 1087 is shown as a bar plot and colored according to the TPR domain in (a). The *in vitro* aggregation
 1088 experiments were performed in triplicate and the data is reported as the average end point with
 1089 standard deviations.

1090
 1091
 1092
 1093
 1094
 1095
 1096
 1097
 1098

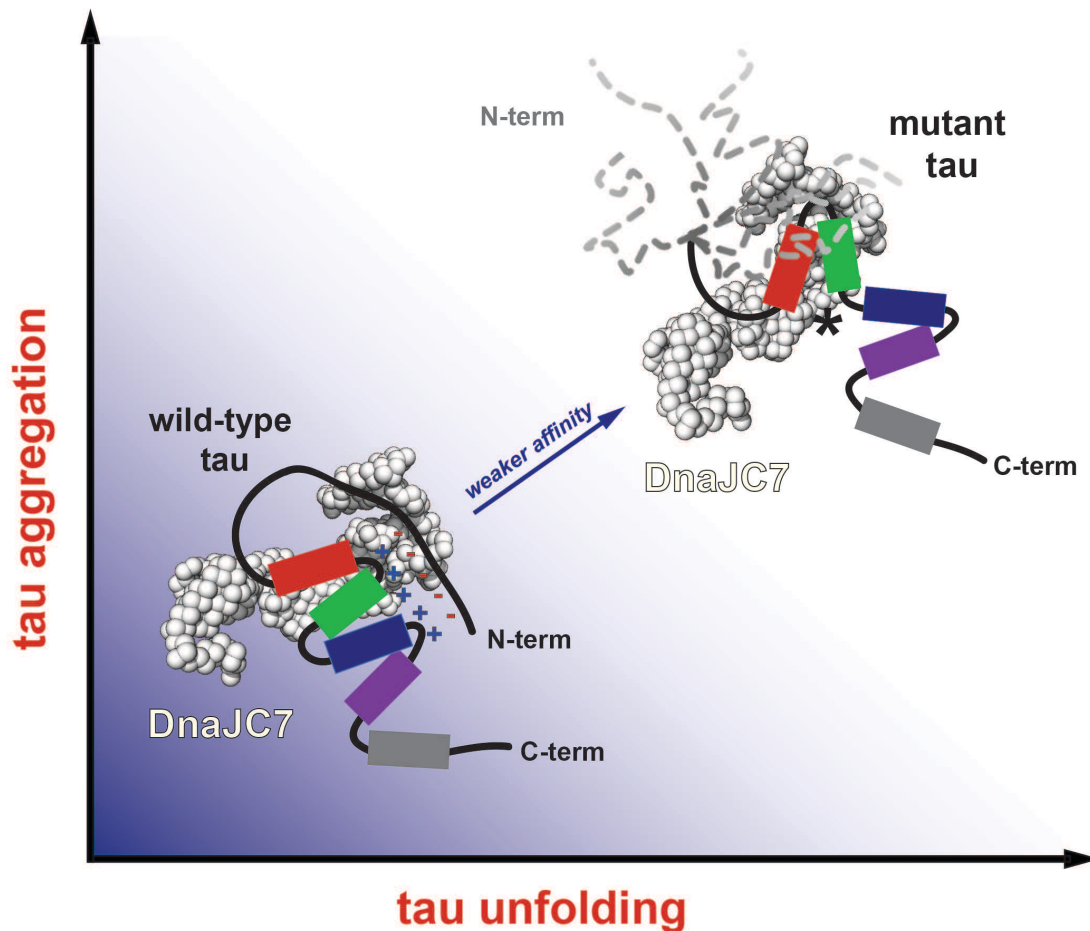


1099
 1100 **Figure 6. DnaJC7 binds to a natively folded conformation of R1R2.** **a.** Schematic illustrating
 1101 the generation of an ensemble of R1R2 peptide conformations used in the DnaJC7 docking
 1102 simulation. The R1R2 peptides are shown in cartoon representation and colored red/green
 1103 according to the repeat domain. **b.** Calculated binding energy and crosslink geometry for the
 1104 R1R2:DnaJC7 structural ensemble. Each point represents a structural model. Models with low
 1105 binding energies and short ca-ca distances between K306 (DnaJC7) and K281 (tau) were used
 1106 in subsequent analyses. **c.** Representative low energy scoring model of DnaJC7 bound to the
 1107 R1R2 peptide. Experimental intramolecular crosslinks observed within R1R2 linking K267-K281,
 1108 K267-K280, K264-K281 and K264-K280 as well as intermolecular contacts between
 1109 K254(TPR2b):K280/K281(tau) and K306(TPR2b):K280/K281(tau) show congruency in our
 1110 docking model and XL-MS identified contacts. DnaJC7 is shown in spacefill representation
 1111 and is colored in grey with TPR2b colored in yellow. R1R2 peptide is shown in cartoon
 1112 representation and is colored in red/green. Crosslink positions are shown as dashed lines
 1113 and colored in blue and orange, respectively. **d.** Mapping the DnaJC7 sequence conservation
 1114 onto the structural model shows that R1R2 binds in a conserved binding groove in TPR2b.
 1115 Conservation is colored from yellow to red. **e.** Mapping the CSPs from Fig. 2a onto the R1R2
 1116 peptide reveals that the surface

1117 on the R1R2 peptide that interact measured by NMR interact with TPR2b surface. CSPs are
1118 colored from yellow (0 ppm) to red (0.04 ppm). **f-g**. Schematic for a competition experiment to
1119 determine whether WT R1R2 (collapsed) or a conformational mutant P270S R1R2 (expanded)
1120 can bind to DnaJC7 and compete binding to tau thereby reducing the capacity of DnaJC7 to
1121 inhibit tau aggregation in a ThT aggregation assay. The bar plot of the three reactions reveals
1122 that the addition of the WT R1R2 peptide (green) can reduce anti-aggregation effect of the
1123 DnaJC7 chaperone, while addition P270S R1R2 (blue) yields nearly identical signal as no
1124 peptide added (black). Experiments were performed in triplicate and are shown as averages with
1125 standard deviation.

1126
1127
1128
1129
1130
1131
1132
1133
1134
1135
1136
1137
1138
1139
1140
1141
1142
1143
1144
1145
1146
1147
1148
1149
1150
1151
1152
1153
1154
1155
1156
1157
1158
1159
1160
1161
1162
1163
1164
1165

Figure 7



1166
1167 **Figure 7. Proposed model of DnaJC7 recognition of natively folded conformations of tau**
1168 **to efficiently suppress amyloid aggregation.** Pathogenic mutations in tau unfold local
1169 conformations in the repeat domain and influence the dynamics of the acidic N-terminal contacts
1170 with the more basic repeat domain (shown as “minus” and “plus” symbols), resulting in structural
1171 rearrangements that yield an aggregation-prone conformation. DnaJC7 binds to the folded R1R2
1172 element in WT tau and efficiently reduces aggregation. This effect is reduced in the aggregation-
1173 prone conformations, such as those found in P301L tau. Tau is colored according to the repeat
1174 domains in red, green, blue and magenta. DnaJC7 is shown in white spheres.
1175

1176
1177
1178
1179
1180

1181

1182

1183

1184

SUPPLEMENTARY INFORMATION

1185

1186 **DnaJC7 binds natively folded structural elements in tau to inhibit amyloid**
1187 **formation**

1188

1189 Zhiqiang Hou, Pawel M. Wydorski, Valerie A. Perez, Aydé Mendoza-Oliva, Bryan D. Ryder, Omar
1190 Kashmer, Hilda Mirbaha, Lukasz A. Joachimiak

1191

1192

1193

1194

1195

1196

1197

1198

1199

1200

1201

1202

1203

1204

1205 **Supplementary Data 1. Primary mass spectrometry analysis of immunoprecipitated tau from PS19**
1206 **mouse brains.**

1207

1208 **Supplementary Data 2. Primary XL-MS data for tauRD:DnaJC7, tau and tau:DnaJC7.**

1209

1210

1211

1212

1213

1214

1215

1216

1217

1218

1219

1220

1221

1222

1223

1224

1225

1226

1227

1228

1229

1230

1231

1232

1233

1234

1235

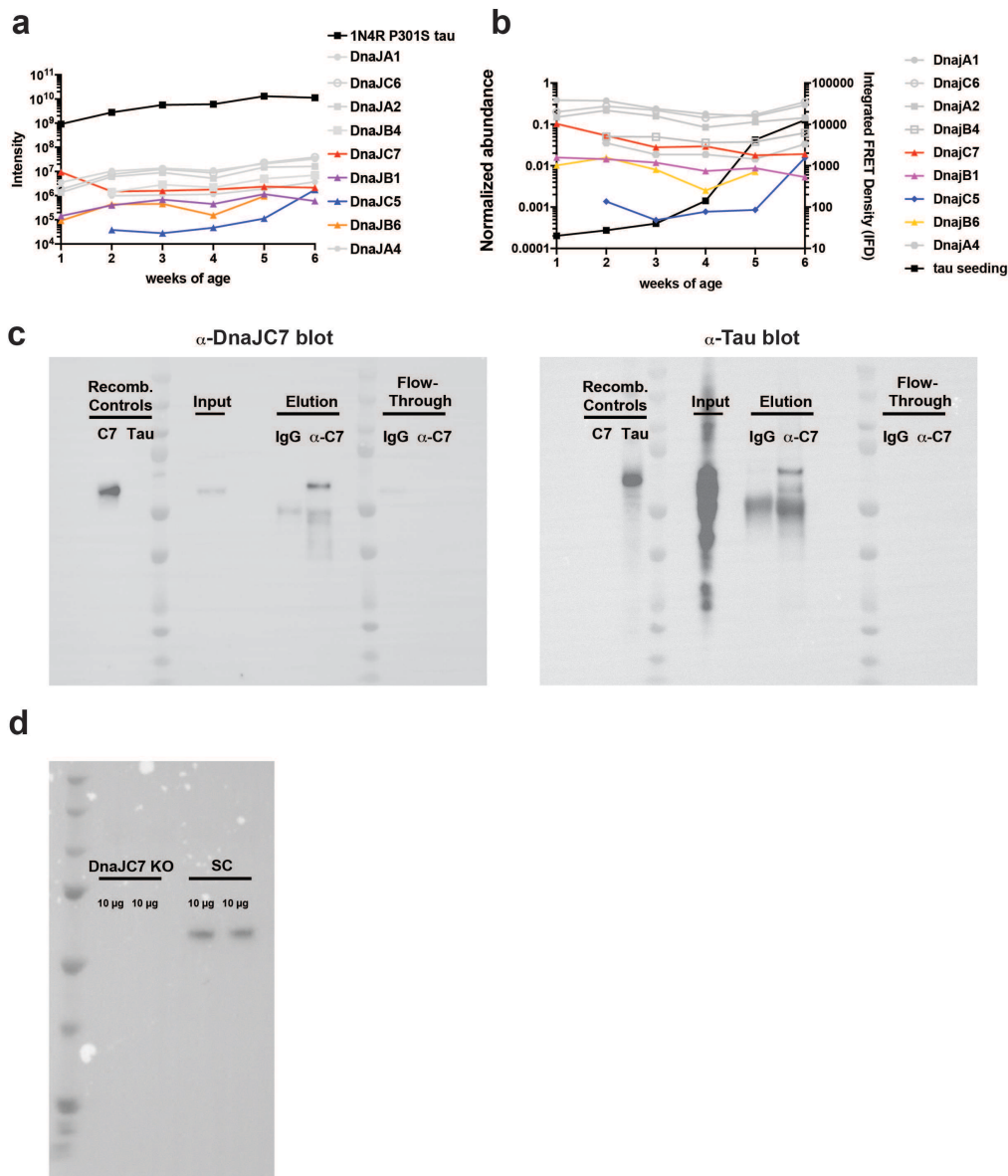
1236

1237 SUPPLEMENTARY TABLES
1238

Target Gene Symbol	Genomic Sequence	Strand	sgRNA Target Sequence	Target Context Sequence
DNAJC7	NC_000017.11	sense	AAATGCTCAGGCACAACAAG	ATAAAAATGCTCAGGCACAACAAGAGGTAC
DNAJC7	NC_000017.11	antisense	CCTTCCAAGCATCATCAAGG	GGAACCTTCCAAGCATCATCAAGGTGGCTG
DNAJC7	NC_000017.11	sense	GCAAGTGCCACCTCTCTCTG	GAGGGCAAGTGCCACCTCTCTCTGGGGAAT
DNAJC7	NC_000017.11	Sense	GCTAAACTCTACTGTAATCG	AAATGCTAAACTCTACTGTAATCGGGGTAC

1239
1240 Supplementary Table 1. CRISPR gRNA sequences used to knock-out DnaJC7.
1241
1242

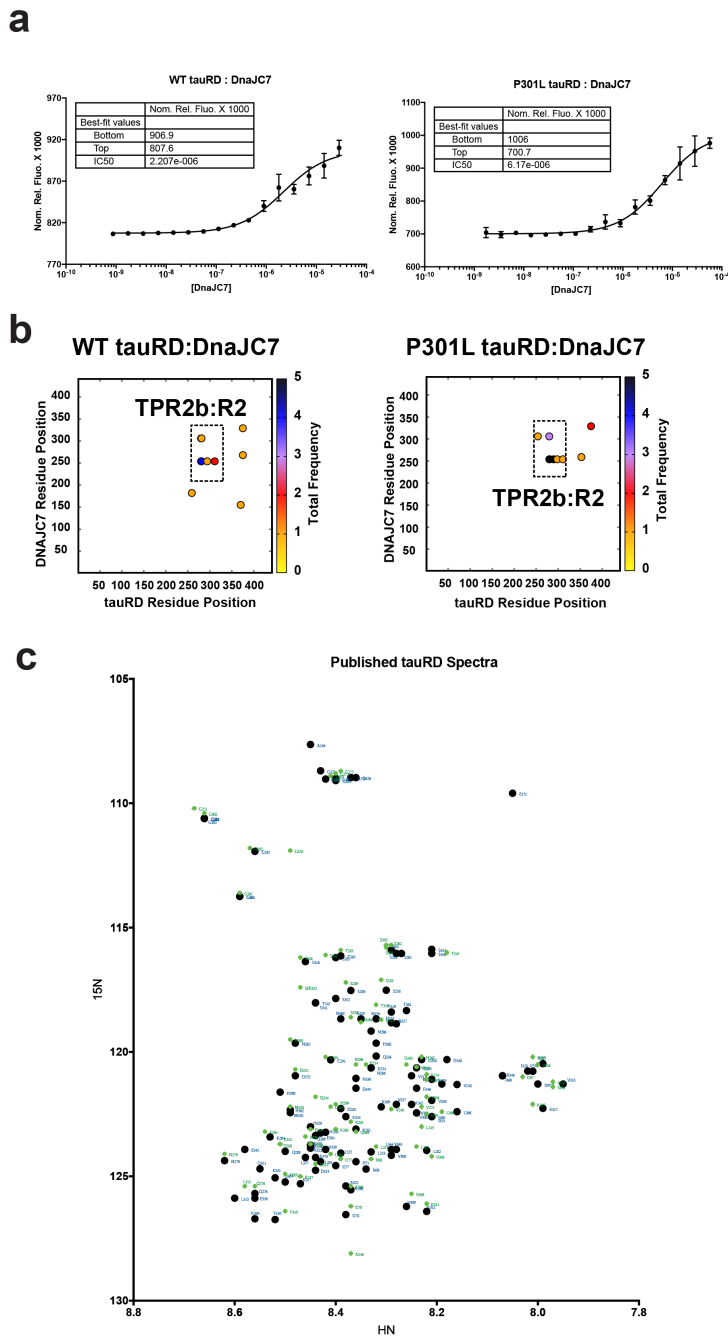
1243
1244
1245
1246
1247
1248
1249
1250
1251
1252
1253
1254
1255
1256
1257
1258
1259
1260
1261
1262
1263
1264
1265
1266
1267
1268
1269
1270
1271
1272
1273
1274
1275
1276
1277
1278
1279
1280
1281



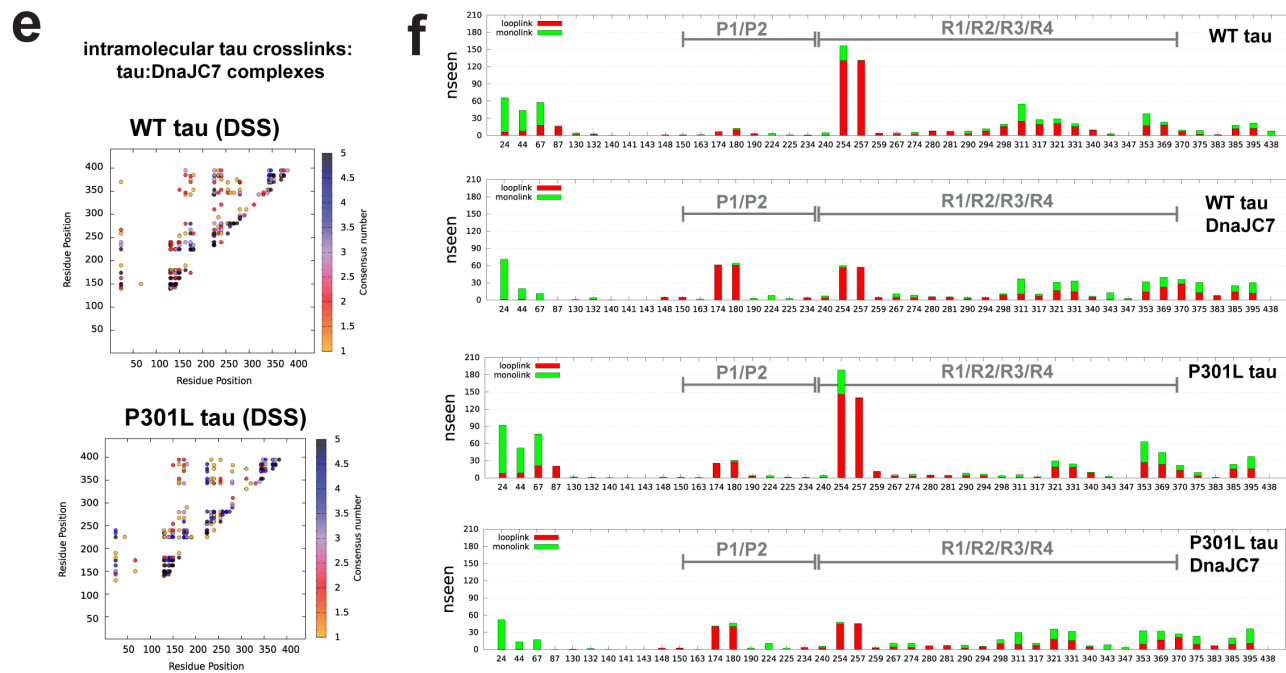
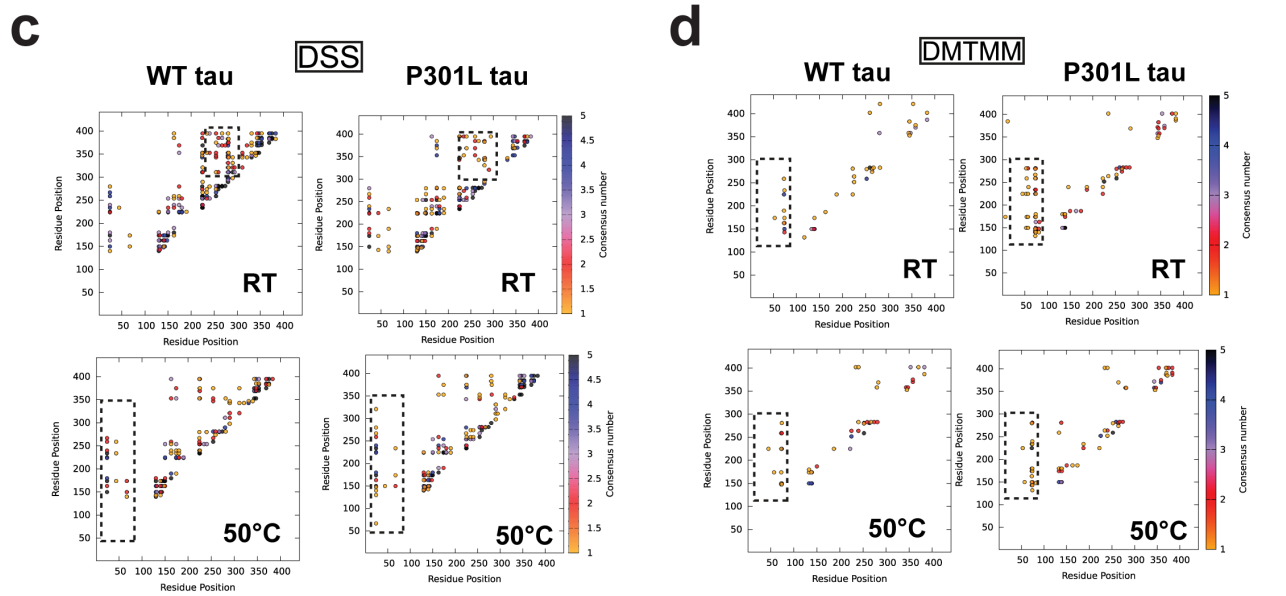
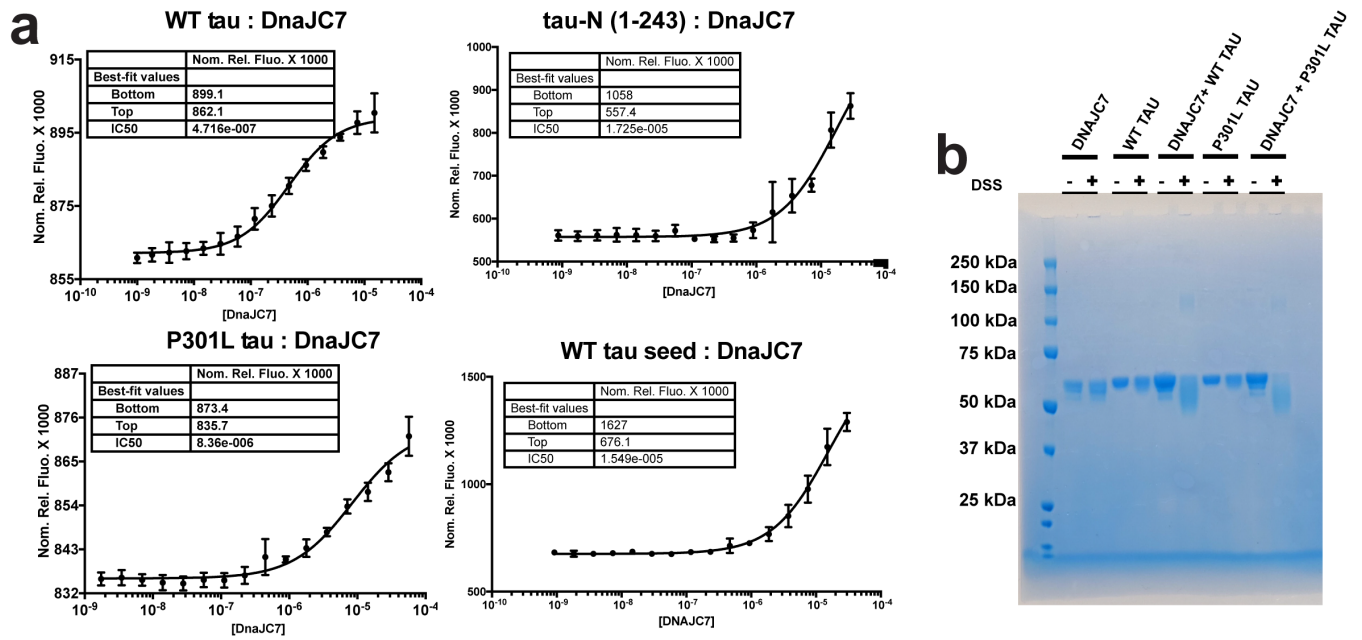
1284
 1285
 1286 **Supplementary Figure 1. Co-Immunoprecipitation of tau and associated Hsp40 chaperones. a.**
 1287 Mass spectrometry analysis of tau immunoprecipitation from PS19 tauopathy mice across different ages
 1288 (weeks 1 through 6) reveals increasing levels of tau (black squares) and identified 9 Hsp40s associated
 1289 with tau in each sample. DnaJA1 (grey closed circles), DnaJC6 (grey open circles), DnaJA2 (grey closed
 1290 squares), DnaJB4 (grey open squares) and DnaJA4 (grey closed hexagons) tracked with tau levels.
 1291 DnaJB6 (closed orange triangles) and DnaJB1 (closed magenta triangles) levels increased but absolute
 1292 levels were low. DnaJC7 (closed red triangles) abundance decreased while DnaJC5 (closed blue
 1293 diamonds) abundance increased. The mass spectrometry data were analyzed using Proteome
 1294 Discoverer (Thermo). Missing points indicate no detectable signal for that Hsp40 was observed (DnaJB4,
 1295 DnaJC5, DnaJB6 and DnaJA4). **b.** The immunoprecipitated tau from PS19 tauopathy mice across
 1296 different ages (weeks 1 through 6) reveals presence of seeds at early ages (black closed squares). The
 1297 levels of Hsp40s were normalized to the signal intensity of tau in each sample. DnaJA1 (grey closed
 1298 circles), DnaJC6 (grey open circles), DnaJA2 (grey closed squares), DnaJB4 (grey open squares) and
 1299 DnaJA4 (grey closed hexagons) remained flat, while DnaJB6 (closed orange triangles), DnaJB1 (closed
 1300 magenta triangles) decreased modestly while DnaJC7 (closed red triangles) decreased dramatically.
 1301 DnaJC5 (closed blue diamonds) abundance increased. Isolated tau from the different samples were
 1302 evaluated for the presence of pathogenic seeds using tau biosensors (right y-axis) and the normalized

1303 abundance of DnaJC7 (relative to P301S 1N4R tau) was determined using mass spectrometry (left y-
1304 axis). Seeding experiments were performed in triplicate. The mass spectrometry data were analyzed
1305 using Proteome Discoverer (Thermo). **c.** Western blots of immunoprecipitations of DnaJC7 from PS19
1306 mouse brains were probed with antibodies against DnaJC7 (left) and tau (right). Each blot contains
1307 recombinant proteins (DnaJC7 and 2N4R tau) as well as inputs (2%), flowthroughs, and elutions for IgG
1308 control and Anti-DnaJC7 immunoprecipitations. Elution fractions contain background signal for anti-
1309 bodies used in the immunoprecipitation (@ ~50kDa) despite using specialized secondary antibodies to
1310 reduce cross reactivity. **d.** Western blots of HEK293T tau biosensor cell lines treated with gRNAs to create
1311 KO DnaJC7 and scrambled non-targeting control cell lines (SC) used in this study.

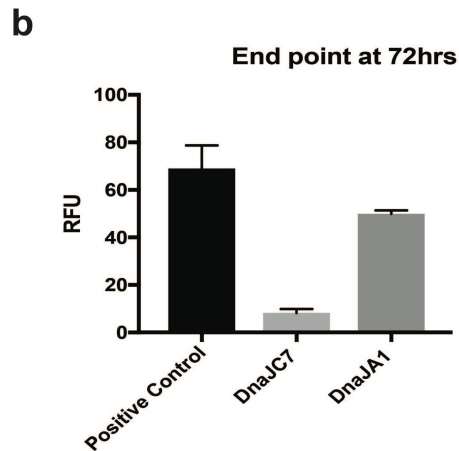
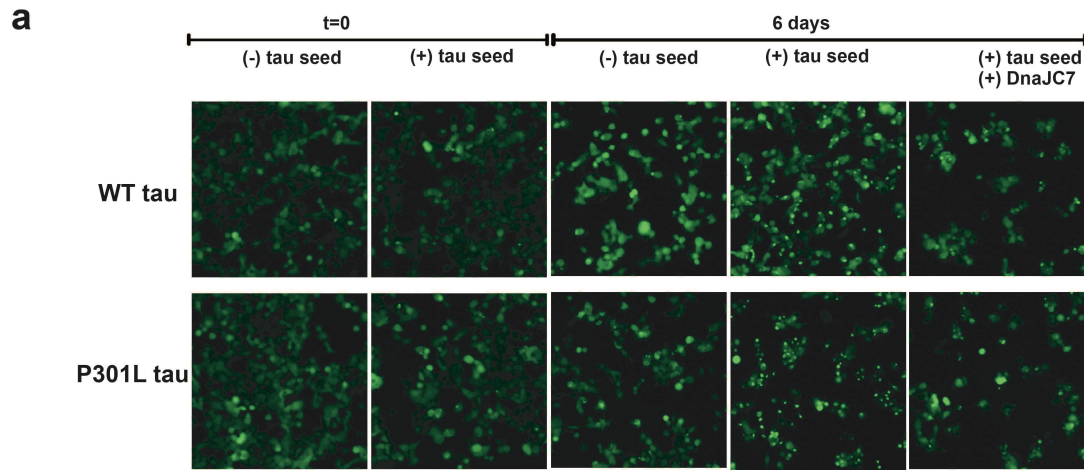
1312
1313
1314
1315
1316
1317
1318
1319
1320
1321
1322
1323
1324
1325
1326
1327
1328
1329
1330
1331
1332
1333
1334
1335
1336
1337
1338
1339
1340
1341
1342
1343
1344
1345
1346
1347
1348
1349
1350
1351
1352



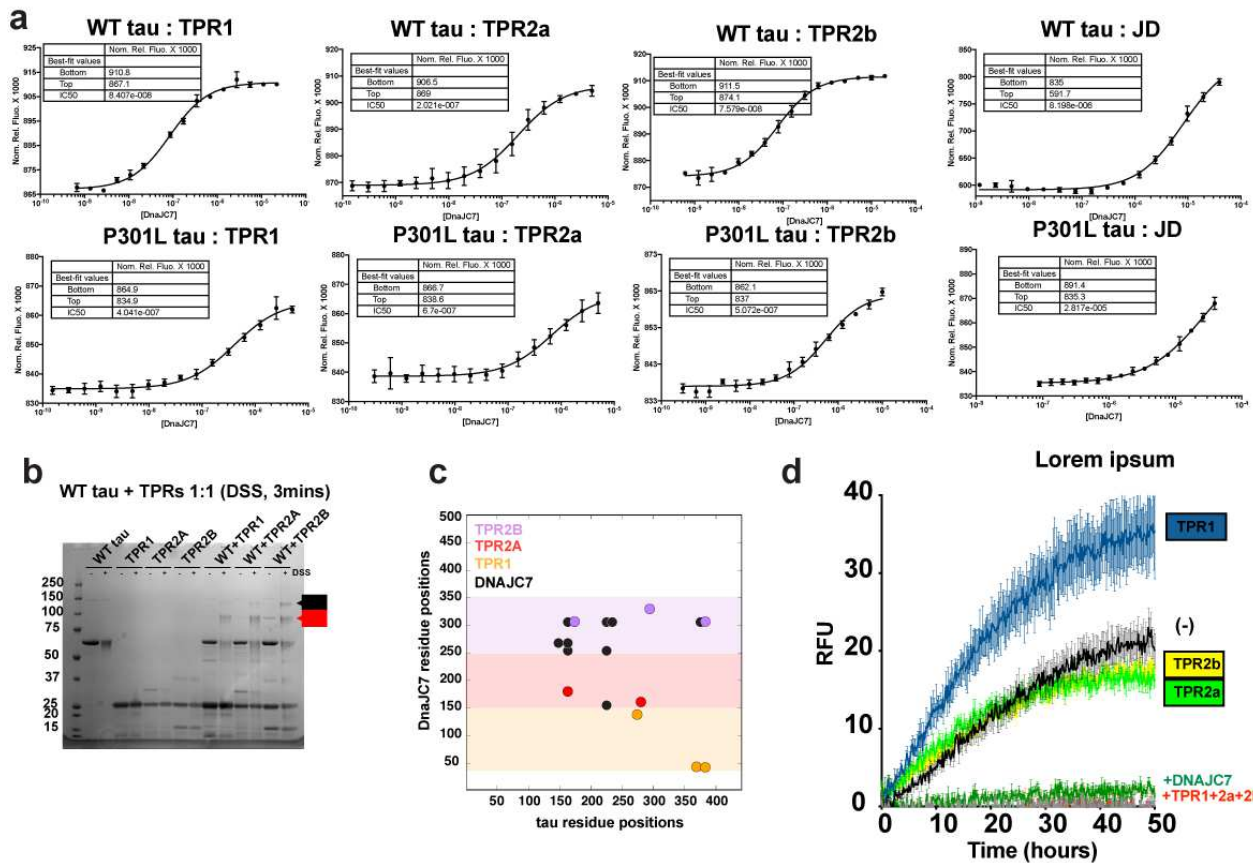
1353
 1354 **Supplementary Figure 2. DnaJC7 binds to R1R2 in tauRD.** **a.** MST analysis of affinity
 1355 between tauRD (WT and P301L) and DnaJC7. TauRD was labeled with Cyanine5 NHS ester
 1356 dye (Cy5) and titrated by a serial two-fold dilution of DnaJC7. The experiments were performed
 1357 in triplicate and each concentration point is shown as an average with standard deviation. The
 1358 data were fit to a linear regression model to estimate the binding constant. **b.** XL-MS to identify
 1359 the contact maps between tauRD (WT and P301L) and DnaJC7. The recombinant WT and
 1360 P301L tauRD were chemically crosslinked with DSS for one minute. After crosslinking, trypsin
 1361 fragmentation and LC-MS analysis were performed. Each sample was carried out in five
 1362 technical replicates. The crosslink pairs (in circles) are colored by average frequency across the
 1363 replicates. **c.** Overlay and amino acid assignments of submitted spectra of K18 245-372 (black,
 1364 BMRB: 19253) and kind gift of K18 243-324 data (green) from Prof. Guy Lippens.
 1365



1367 **Supplementary Figure 3. DnaJC7 prefers binding to natively folded tau.** **a.** MST analysis
1368 of binding affinity between WT tau:DnaJC7, P301L tau:DnaJC7, N-term tau (1-243):DnaJC7 and
1369 tau seed:DnaJC7. WT tau, P301L tau, N-term tau and tau seed were labeled with Cyanine5
1370 NHS ester dye (Cy5) and titrated by a serial two-fold dilution of DnaJC7. The experiments were
1371 performed in triplicate and each concentration point is shown as an average with standard
1372 deviation. The data were fit to a linear regression model to estimate the binding constant. **b.**
1373 SDS-PAGE Coomassie gel of crosslinked WT tau:DnaJC7 and P301L tau:DnaJC7 complex with
1374 DSS. Only the bands containing DnaJC7 and tau were cut out for gel extraction followed by XL-
1375 MS analysis. **c-d.** Consensus crosslink pairs of full-length WT/P301L tau (in circles) are shown
1376 in contact maps colored by average frequency across replicates using chemical reagent DSS
1377 (**c**) and DMTMM (**d**). In control, recombinant WT and P301L tau were heated at 50°C for one
1378 hour, then chemically crosslinked with DSS or DMTMM for one minute. After crosslinking, gel
1379 extraction, trypsin fragmentation, and LC-MS analysis were performed. Each sample was carried
1380 out in five technical replicates. The dashed boxes emphasize the paired differences between
1381 WT and P301L tau. **e.** Consensus contact map of tau (WT, P301L) intramolecular crosslinks
1382 identified from the tau:DnaJC7 complexes colored by average frequency across replicates. **f.**
1383 Histogram of average frequencies of mono- and loop- crosslinks across replicates for WT tau in
1384 isolation and from the complex and P301L tau in isolation and from the complex. Monolinks and
1385 looplinks are in green and red, respectively. P1/P2 and repeat domain regions are highlighted
1386 with brackets.
1387
1388
1389
1390
1391
1392
1393
1394
1395
1396
1397
1398
1399
1400
1401
1402
1403
1404
1405
1406
1407
1408
1409
1410
1411
1412
1413
1414
1415
1416

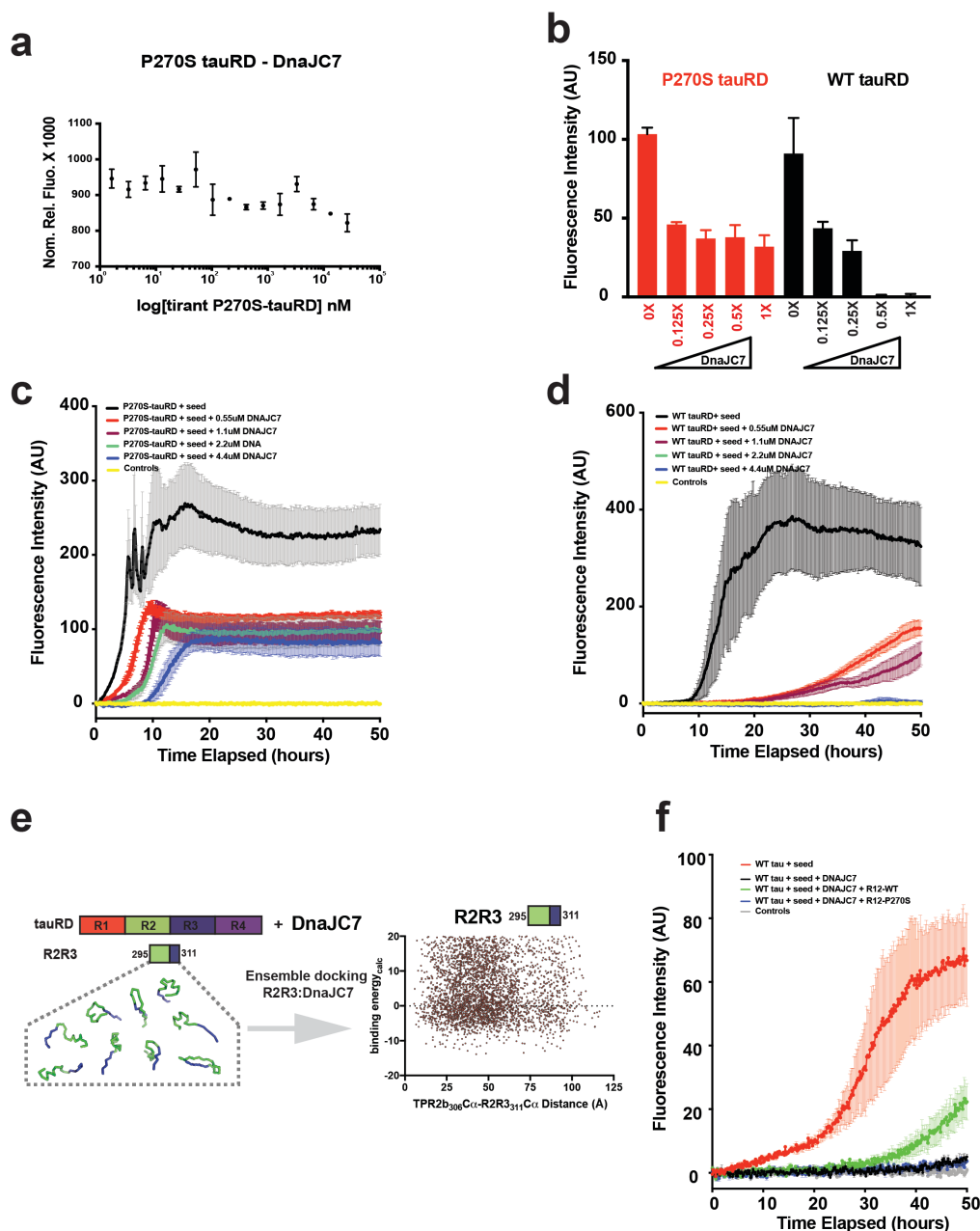


1417
 1418
 1419 **Supplementary Figure 4. DnaJC7 suppression of tau aggregation does not produce**
 1420 **seeds.** **a.** Seeding activity in tau RD-CFP/YFP biosensor cells. Full-length tau (WT and P301L)
 1421 incubated with Ms or DnaJC7 from previous ThT experiments were seeded into cells via
 1422 lipofectamine transfection (Methods) at Day 0 (T0) and Day 6 (T6). At T0, WT and P301L tau
 1423 only show background FRET signal from Ms. At T6, both WT and P301L exhibit strong seeding
 1424 activity in condition with Ms but decreased activity in condition with Ms and DnaJC7. All seeding
 1425 experiments were carried out in triplicate. **b.** Specificity between DnaJC7 and canonical DnaJ
 1426 family member proteins attributed to tau anti-aggregation effects. After 72 hours incubation, tau
 1427 incubated with different DnaJ proteins were transduced into biosensor cells. FRET (tau RD-
 1428 mClover/mCerulean) from each condition was measured by flow cytometry in triplicates with
 1429 standard deviation.
 1430



1431
 1432 **Supplementary Figure 5. DnaJC7's anti-aggregation activity relies on all three TPR**
 1433 **domains.** **a.** MST analysis of affinity between WT tau with DnaJC7 domains (upper panel) and
 1434 P301L tau with DnaJC7 domains (lower panel). WT tau and P301L tau were labeled with
 1435 Cyanine5 NHS ester dye (Cy5) and titrated by a serial two-fold dilution of DnaJC7 domains. The
 1436 experiments were done in triplicate and shown as an average with standard deviation. **b.** SDS-
 1437 PAGE Coomassie gel of crosslinked TPR domain:tau complex. Recombinant TPR domains and
 1438 full-length WT tau were incubated at RT for one hour then chemically cross-linked using DSS.
 1439 Only the bands forming complex (red mark) are cut out for gel extraction followed by XL-MS
 1440 analysis. **c.** Overlay contact map of DSS crosslinks identified for each single TPR domain:WT
 1441 tau to full-length WT tau:DnaJC7. The crosslink pairs are colored by domain TPR1 (yellow),
 1442 TPR2a (red), TPR2b (purple) and full-length DnaJC7 (black). The y-axis is colored according to
 1443 DnaJC7 domain. The TPR2b: WT tau crosslink pairs recapitulate the contacts observed in full-
 1444 length DnaJC7. **d.** ThT experiment that shows that a single TPR domain is not sufficient to
 1445 depress tau aggregation. Full-length DnaJC7 or combination of three TPRs efficiently depress
 1446 the tau aggregation. 4.4 μ M P301L tau aggregation was induced using 50 nM tau seeds in the
 1447 presence of different DnaJC7 TPR domains. Aggregation was monitored via ThT fluorescence.
 1448 Experiments were performed in triplicate and are shown as averages with standard deviation.
 1449 Individual DnaJC7 domains were added in an equimolar ratio to tau.

1450
 1451
 1452
 1453
 1454
 1455
 1456
 1457



1458
 1459 **Supplementary Figure 6. P270S mutation in R1R2 prevent recognition by DnaJC7.** **a.** MST
 1460 analysis shows no binding affinity between P270S tau RD with DnaJC7. DnaJC7 was labeled
 1461 with Cyanine5 NHS ester dye (Cy5) and titrated by a serial two-fold dilution of P270S tauRD.
 1462 The experiments were done in triplicate and shown as an average with standard deviation. **b.**
 1463 Bar plot of end point values (@50 hours) for seeded aggregation kinetics of 4.4uM P270S tauRD
 1464 (red) and 4.4uM WT tauRD (black) in the presence of 0X, 0.125X, 0.25X, 0.5X and 1X DnaJC7
 1465 concentrations. **(c-d)** Raw ThT aggregation traces of P270S tauRD and WT tauRD in the
 1466 presence of increasing concentrations of DnaJC7 over 50 hours. ThT signals are an average of
 1467 three independent experiments with standard deviation. **e.** Schematic illustrating the generation
 1468 of an ensemble of R2R3 peptide conformations used in the DnaJC7 docking simulation. The
 1469 R2R3 peptides are shown in cartoon representation and colored green/blue according to the
 1470 repeat domain. Calculated binding energy and crosslink geometry for the R2R3:DnaJC7
 1471 structural ensemble. Each point represents a structural model. Models with low binding energies
 1472 and short C α -C α distances between K306 (DnaJC7) and K311 (tau) were used in subsequent
 1473 analyses. **f.** ThT aggregation reactions of 4.4uM WT tau, 50nM tau monomer seeds and 4.4uM
 1474 DnaJC7 in the presence of buffer (black), P270S peptide R1R2 (blue), WT peptide R1R2

1475 (green). Control 4.4uM WT tau with 50nM tau monomer seeds is shown in red. Individual
1476 component controls are shown in grey. ThT signals are an average of three independent
1477 experiments with standard deviation.

Figures

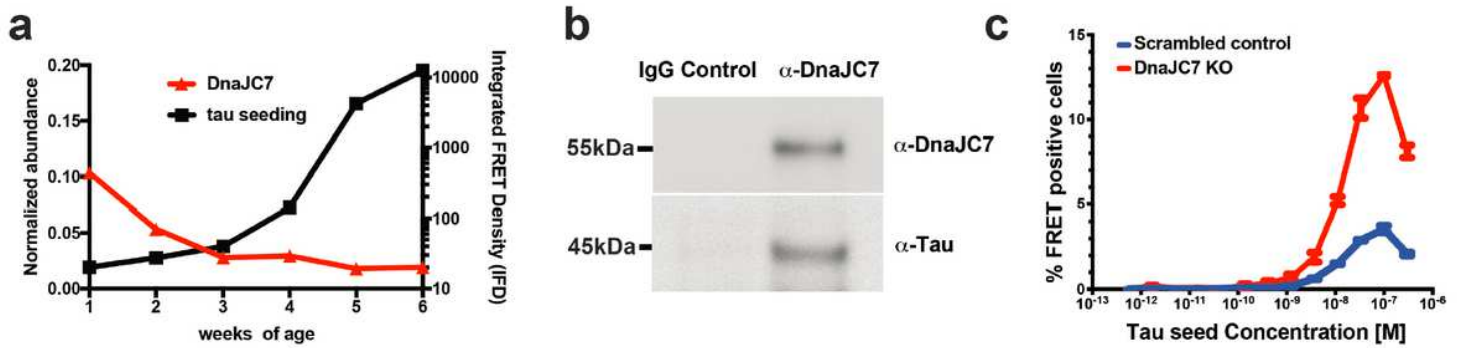


Figure 1

Identification of a novel Hsp40 DnaJC7 that binds to tau and influences seeding. a. Immunoprecipitation of tau from PS19 tauopathy mice across different ages (weeks 1 through 5) reveals an increase in seeding activity at early ages (black) which anti-correlates with a 5-fold decrease of Hsp40 DnaJC7 abundance (red). Isolated tau from the different samples were evaluated for the presence of pathogenic seeds using tau biosensors (right y-axis) and the normalized abundance of DnaJC7 (relative to P301S 1N4R tau; $[Hsp40/Itau]*100$) was determined using mass spectrometry (left y-axis). Seeding experiments were performed in triplicate and the mass spectrometry data were analyzed using Proteome Discoverer (Thermo). b. Co immunoprecipitation of DnaJC7 and tau from PS19 mouse brain lysates. Brain lysates were immunoprecipitated with an anti-DnaJC7 antibody or an IgG antibody as negative control. The immunoprecipitates were analyzed by Western blot analysis and probed with anti-DnaJC7 or anti-tau antibodies. c. Dose titration of recombinant heparin-induced tau fibril seeding on the tauRD mClover3/mCerulean biosensor cells. Cells were treated with tau fibril concentrations performed as three-fold dilutions ranging from 300 nM down to 565 fM. Seeding was quantified via flow cytometry based on the percentage of FRET-positive cells in each sample. The decrease in seeding at 300 nM corresponds to cell death due to toxicity of high concentrations of tau fibrils. Seeding experiments were performed in triplicate and are shown as averages with standard deviation.

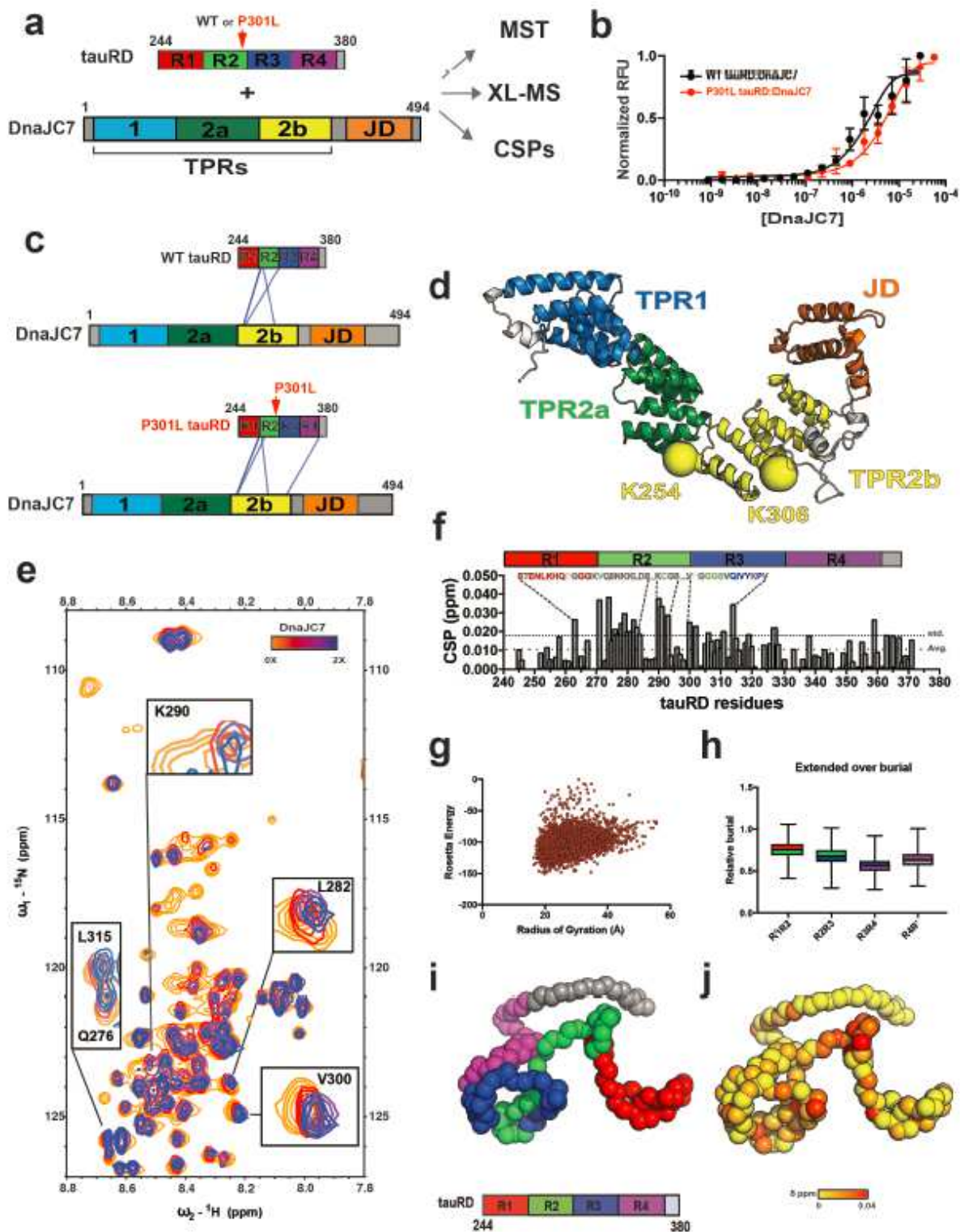


Figure 2

DnaJC7 binds directly to tauRD through the R1R2 inter-repeat element. a. Schematic representation of the DnaJC7 and tauRD constructs used to probe their interaction. TauRD domains are colored in red, green, blue and magenta for repeats 1, 2, 3 and 4, respectively. DnaJC7 domains are colored in light blue, dark green, yellow and orange for TPR1, TPR2a, TPR2b and J-domain, respectively. b. MST assay to quantify affinity between tauRD (WT and P301L) and DnaJC7. The tauRD:DnaJC7 and P301L tauRD:DnaJC7

binding curves are colored in black and red, respectively. The MST binding experiments were performed in triplicate and each concentration point is shown as an average with standard deviation. The data were fit to a linear regression model to estimate the binding constant. c. XL-MS to identify the interactions in the complex. Each protein is shown as cartoon schematic and the crosslinks are shown as blue lines linking the two crosslinked positions. The constructs are colored as in (a). d. DnaJC7 homology model shown in cartoon representation and the domains are colored as in (a). The two major crosslink sites in TPR2b are shown as spheres and colored by the domain. e. 2D ^1H - ^{15}N HSQC spectra of tauRD in the absence (red) and in the presence of increasing DnaJC7 concentrations. Molar ratio of tauRD to DnaJC7 is 2:1 (yellow), 1:1 (red), 1:2 (blue). Key peaks that are significantly perturbed in the presence of DnaJC7 are shown as insets and labeled by the amino acid position. f. NMR CSPs of tauRD in 1:1 molar ratio of DnaJC7 are shown as a bar plot colored in grey. The amino acid residues for tauRD that are significantly shifted are shown above the bar plot, the remaining residues are colored as in (a). The tauRD cartoon is shown above the plot and the domains are colored as in (a). Residues that are significantly perturbed are consistent with the region identified by XL-MS. Average and standard deviations are shown as dashed lines. g. Left panel, Rosetta Energy and calculated radius of gyration is shown for an ensemble of tauRD models built by CS-ROSETTA. h. Ensemble average of normalized solvent exposure (normalized to solvent exposure of a fully extended chain) for inter repeat elements R1R2, R2R3, R3R4 and R4R' is shown as a box plot and colored red/green, green/blue, blue/magenta and magenta/grey, respectively. Consistent with DnaJC7 the R1R2 element appears most exposed. i. Representative model of tau RD from the ensemble highlights relative exposure of the R1R2 element. The backbone of the model is shown in spacefill and is colored as in (a). j. The backbone of the model is shown in spacefill and shown in the same orientation as (i). tauRD model is colored according to DnaJC7-induced CSPs color-coded from yellow (0 ppm) to red (0.04 ppm).

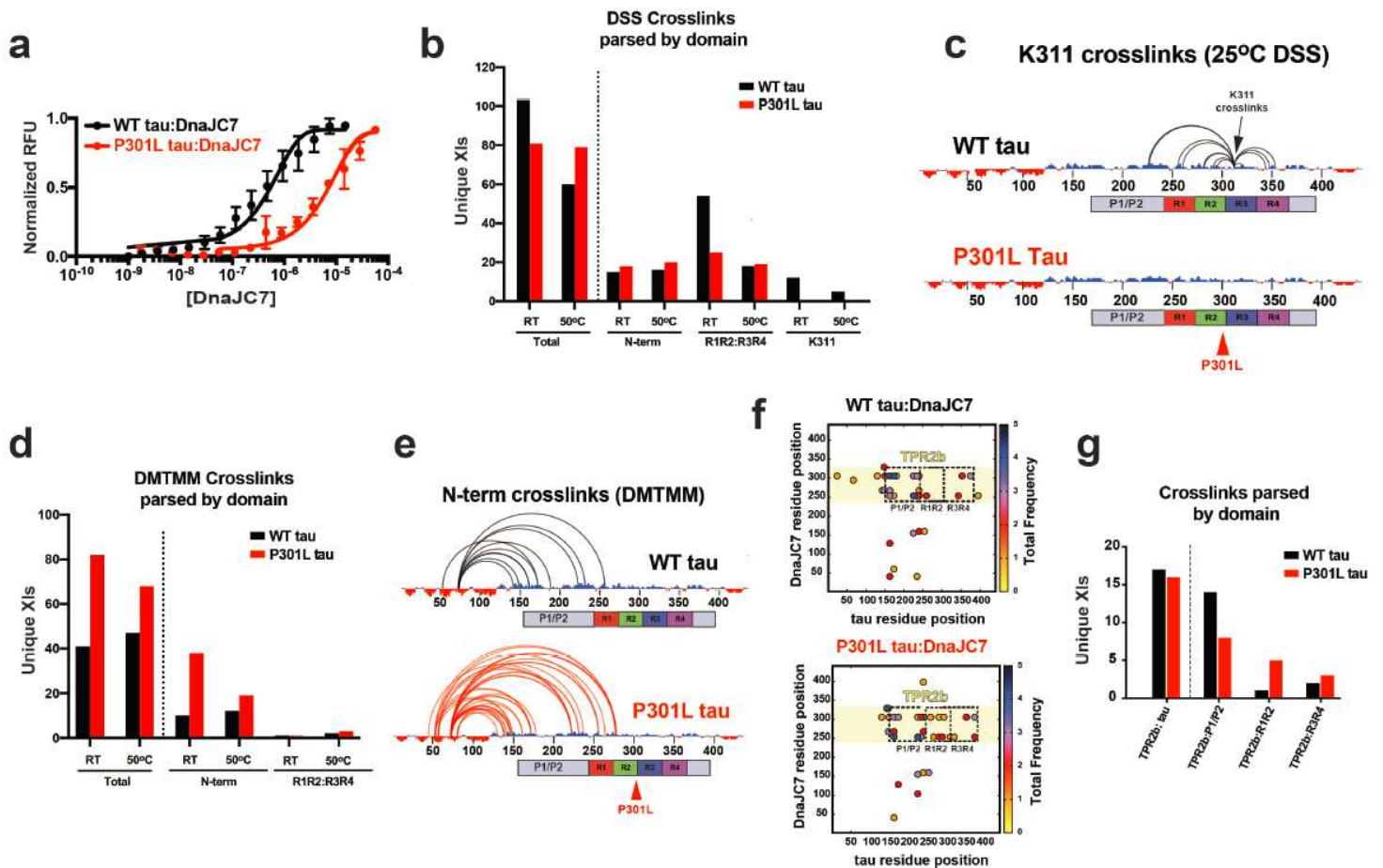


Figure 3

Pathogenic P301L mutation alters tau dynamics and impacts DnaJC7 binding affinity. **a**. MST to quantify affinity of full-length tau (WT/P301L) and DnaJC7. The WT tau:DnaJC7 and P301L tau:DnaJC7 binding curves are colored in black and red, respectively. The MST binding experiments were performed in triplicate and are shown as an average with standard deviation. The data were fit to a linear regression model to estimate the binding constant. **b**. Unique consensus DSS crosslink pairs identified in WT and P301L tau are shown as a bar plot comparing total crosslinks and crosslinks parsed by different domains (N-terminus, R1R2:R3R4 and K311) and acquired at RT and 50°C. Changes in the distribution of crosslinks across the domains in tau highlight differences in conformation. WT tau and P301L tau crosslinks are colored in black and red, respectively. **c**. Consensus crosslinks involving K311 are shown for WT and P301L tau. The P301L mutation abolishes crosslinks to K311 disfavoring the local compact structure as measured by the absence of crosslinks at K311 in proximity to the mutation. The crosslinks are shown as semi-circles mapped onto the linear sequence of tau. The net charge per residue (NCPR) distribution is shown on the sequence axis to highlight regions with predominantly acidic (red) or basic (blue) sequence elements. Cartoon domain for tau is shown below the sequence axis, the domains are colored as in Fig. 2a. **d**. Unique consensus DMTMM crosslink pairs identified in WT and P301L tau are shown as a bar plot comparing total crosslinks and crosslinks parsed by different domains (N-terminus and R1R2:R3R4) and acquired at RT and 50°C. Changes in the distribution of crosslinks across the domains in tau highlight differences in the conformation of the N-terminal contacts. WT tau and P301L

tau crosslinks are colored in black and red, respectively. e. Consensus crosslinks between the acidic N-terminus and the basic regions of tau (mostly repeat domain). The P301L mutation dramatically increases the heterogeneity of acidic-basic contacts from the N-terminus to the repeat domain compared to WT tau. The crosslinks are shown as semi-circles mapped onto the linear sequence of tau and are colored black and red for WT and P301L tau, respectively. NCPR distribution is shown on the sequence axis to highlight regions with predominantly acidic (red) or basic (blue) sequence elements. Cartoon domain for tau is shown below the sequence axis, the domains are colored as in Fig. 2a. f. Consensus WT tau:DnaJC7 (top) and P301L tau:DnaJC7 (bottom) inter-molecular DSS crosslink contact map colored by average frequency across replicates. TPR2b dominates the contacts with tau but the contacts are differentially redistributed across P1/P2 and R1R2 for WT tau and P301L tau. g. Unique consensus DSS crosslink pairs identified in WT tau:DnaJC7 and P301L tau:DnaJC7 are shown as a bar plot comparing total crosslinks and crosslinks parsed by DnaJC7 TPR2b contacts to different regions on tau (N-terminus, R1R2 and R3R4). In WT tau, tighter binding to DNAJC7 buries R1R2 and exposes P1P2 domain, hence, leading to decreased crosslinks in R1R2 and increased crosslinks in P1P2. WT tau and P301L tau crosslinks are colored in black and red, respectively.

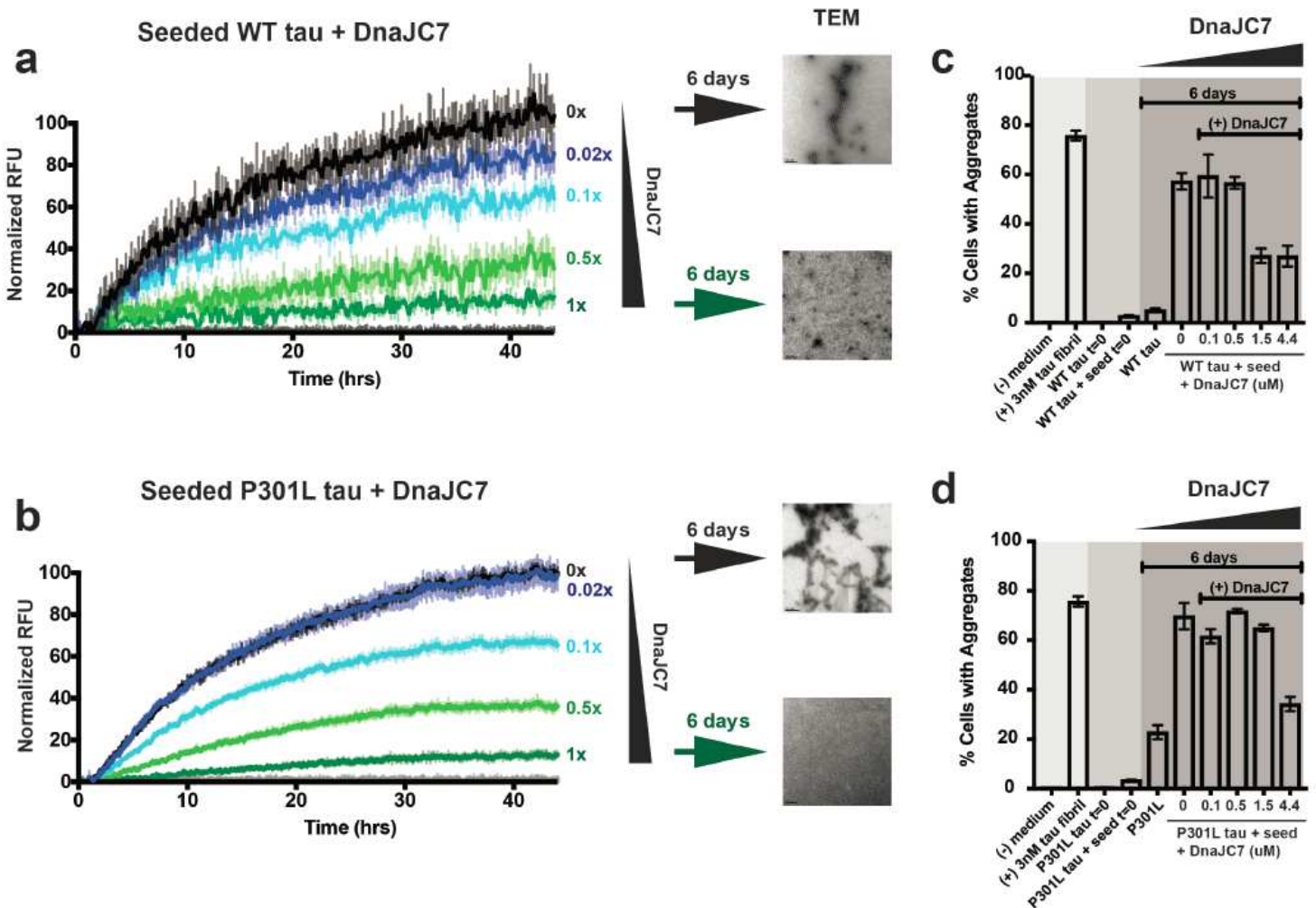


Figure 4

DnaJC7 efficiently suppresses tau aggregation in vitro. 4.4 μ M WT tau (a) and 4.4 μ M P301L tau (b) aggregation was induced using 50nM tau monomer seeds in the presence of different DnaJC7 chaperone concentrations. Aggregation was monitored using ThT fluorescence. Experiments were performed in triplicate and are shown as averages with standard deviation. DnaJC7 concentrations ranged from 0X (0uM), 0.02X (0.1uM), 0.1X (0.5uM), 0.35X (1.5uM), to 1X (4.4uM) and are colored from black to green. Grey curves show negative controls: tau alone, DnaJC7 alone at each concentration and tau monomer seeds alone. TEM images were taken at the end point to confirm the presence or absence of fibrils. (c d) The endpoint and control samples of the in vitro aggregation experiment were assayed for seeding activity in tau biosensors cells. The in-cell aggregation assay shows significant reduction in seeding in the presence of DnaJC7 even after 6 days of incubation and is consistent with the in vitro measurements. Tau seeding experiments were performed in triplicate and are shown as averages with standard deviation.

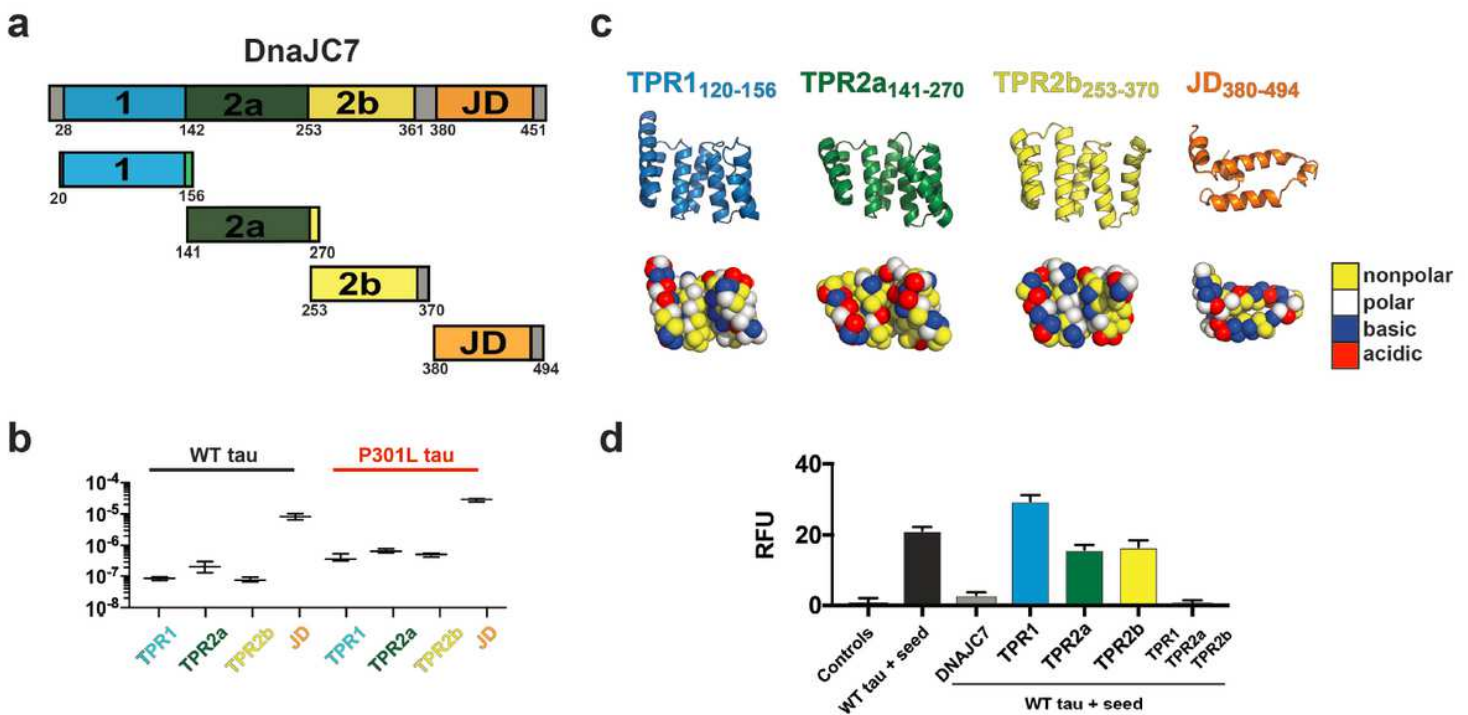


Figure 5

Efficient DnaJC7 suppression of tau aggregation relies on all three TPR domains. a. Schematic diagram of DnaJC7 domain constructs used: TPR120-156 (light blue), TPR2a141-270 (dark green), TPR2b253-370 (yellow) and JD380-494 (orange). b. MST binding affinity summary of TPR construct WT tau and P301L tau. Binding experiments were performed in triplicate and fitted to linear regression curve to estimate binding constants. The derived binding constants are shown as averages with standard deviations across replicate experiments. WT tau and P301L tau binding experiments are shown in black and red, respectively and the TPR labels are colored according to the TPR domain as in (a). c. Cartoon representation of TPR120-156 (light blue), TPR2a141-270 (dark green), TPR2b253-370 (yellow) and JD380-494 (orange) oriented to highlight the peptide binding groove. Spacefill representation of each domain is colored according to amino acid properties; polar (white), nonpolar (yellow), acidic (red) and

basic (blue) residues. d. Individual TPR domains were used in a ThT Fluorescence aggregation assay to measure their effect on suppressing tau aggregation in vitro. The end point of each experiment is shown as a bar plot and colored according to the TPR domain in (a). The in vitro aggregation experiments were performed in triplicate and the data is reported as the average end point with standard deviations.

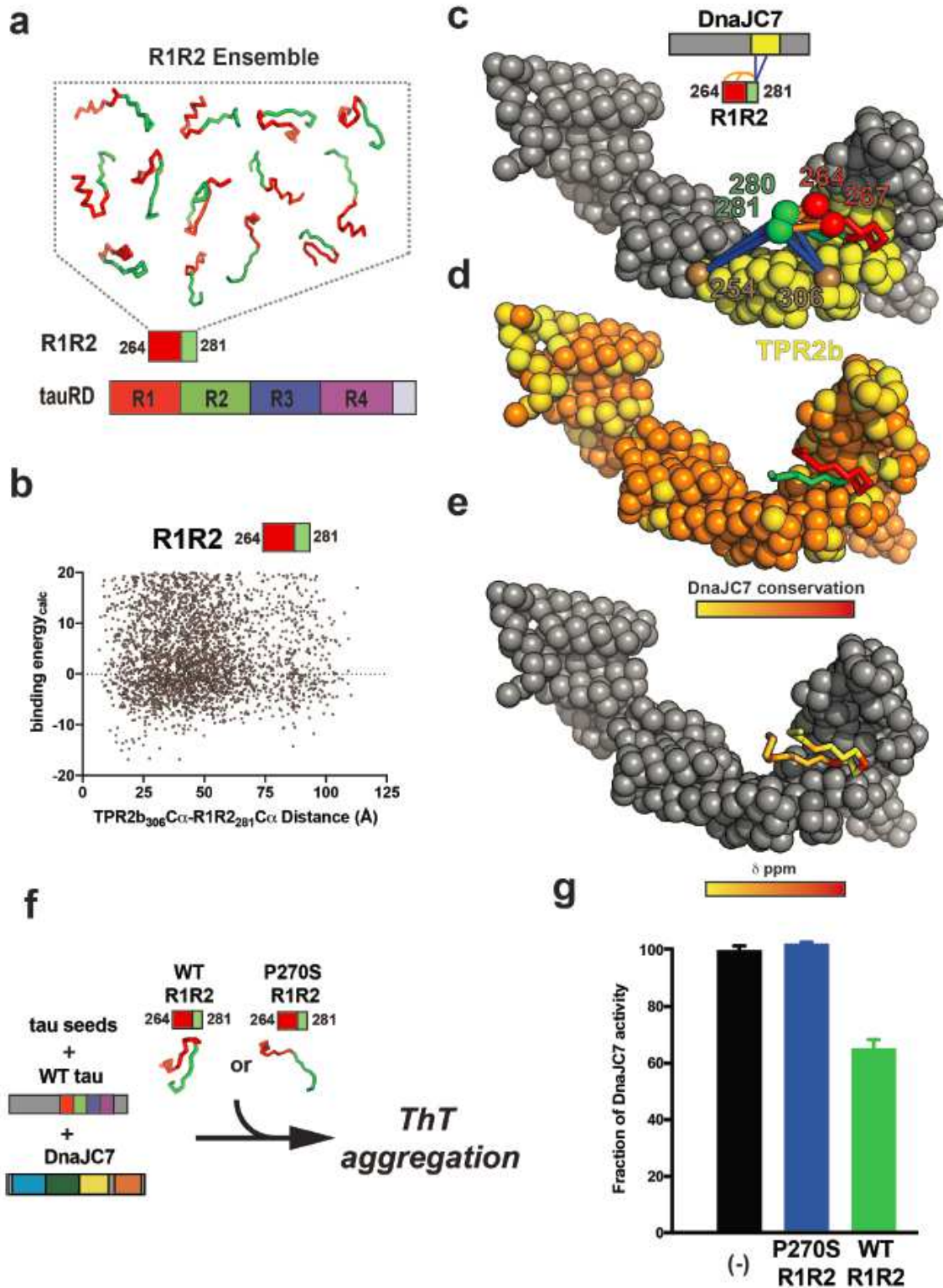


Figure 6

DnaJC7 binds to a natively folded conformation of R1R2. a. Schematic illustrating the generation of an ensemble of R1R2 peptide conformations used in the DnaJC7 docking simulation. The R1R2 peptides are shown in cartoon representation and colored red/green according to the repeat domain. b. Calculated binding energy and crosslink geometry for the R1R2:DnaJC7 structural ensemble. Each point represents a structural model. Models with low binding energies and short ca-ca distances between K306 (DnaJC7) and K281 (tau) were used in subsequent analyses. c. Representative low energy scoring model of DnaJC7 bound to the R1R2 peptide. Experimental intramolecular crosslinks observed within R1R2 linking K267-K281, K267-K280, K264-K281 and K264-K280 as well as intermolecular contacts between K254(TPR2b):K280/K281(tau) and K306(TPR2b):K280/K281(tau) show congruency in our docking model and XL-MS identified contacts. DnaJC7 is shown in spacefill representation and is colored in grey with TPR2b colored in yellow. R1R2 peptide is shown in cartoon representation and is colored in red/green. Crosslink positions are shown in spacefill representation. Intramolecular and intermolecular crosslinks are shown as dashed lines and colored in blue and orange, respectively. d. Mapping the DnaJC7 sequence conservation onto the structural model shows that R1R2 binds in a conserved binding groove in TPR2b. Conservation is colored from yellow to red. e. Mapping the CSPs from Fig. 2a onto the R1R2 peptide reveals that the surface on the R1R2 peptide that interact measured by NMR interact with TPR2b surface. CSPs are colored from yellow (0 ppm) to red (0.04 ppm). f-g. Schematic for a competition experiment to determine whether WT R1R2 (collapsed) or a conformational mutant P270S R1R2 (expanded) can bind to DnaJC7 and compete binding to tau thereby reducing the capacity of DnaJC7 to inhibit tau aggregation in a ThT aggregation assay. The bar plot of the three reactions reveals that the addition of the WT R1R2 peptide (green) can reduce anti-aggregation effect of the DnaJC7 chaperone, while addition P270S R1R2 (blue) yields nearly identical signal as no peptide added (black). Experiments were performed in triplicate and are shown as averages with standard deviation.

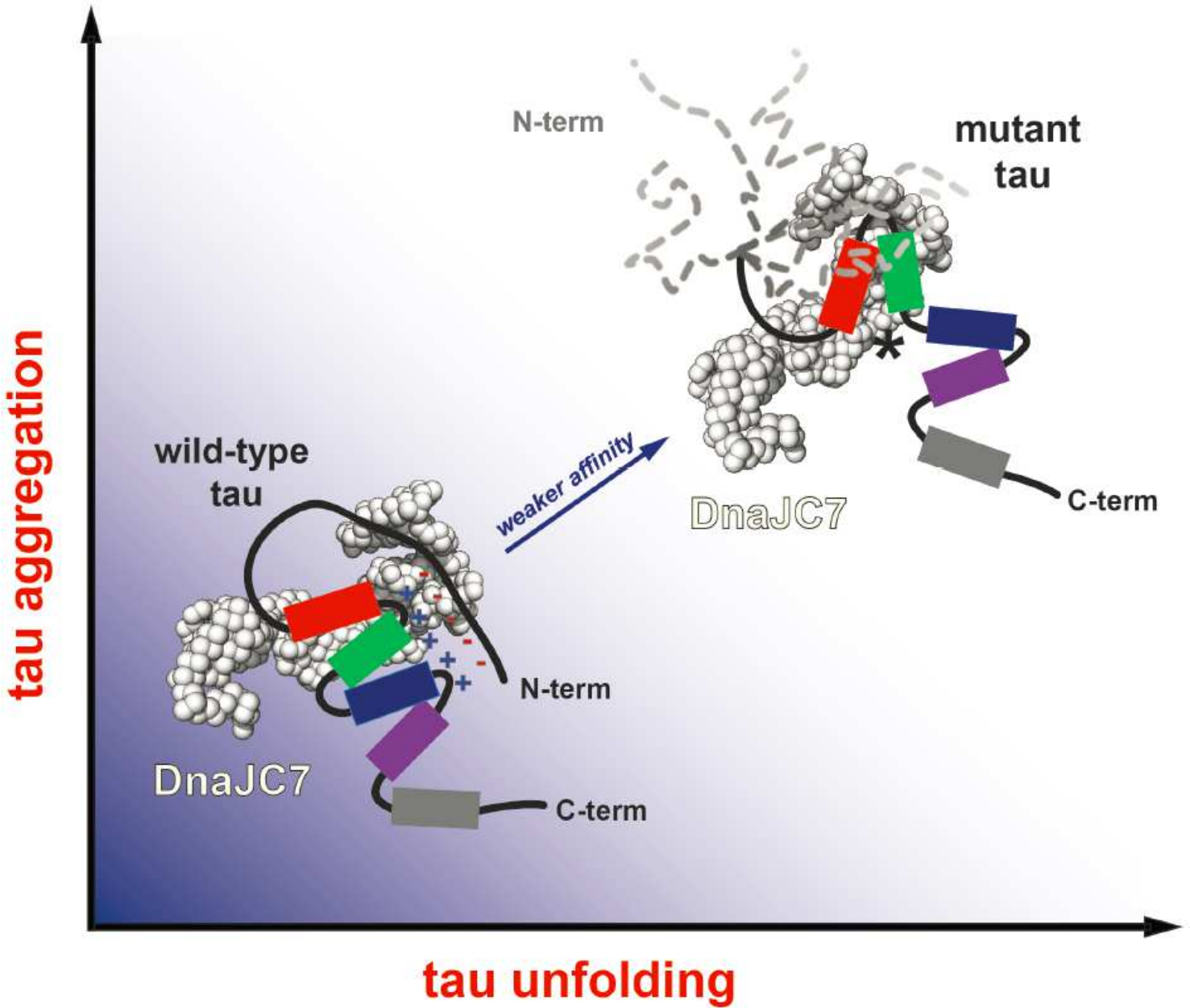


Figure 7

Proposed model of DnaJC7 recognition of natively folded conformations of tau to efficiently suppress amyloid aggregation. Pathogenic mutations in tau unfold local conformations in the repeat domain and influence the dynamics of the acidic N-terminal contacts with the more basic repeat domain (shown as “minus” and “plus” symbols), resulting in structural rearrangements that yield an aggregation-prone conformation. DnaJC7 binds to the folded R1R2 element in WT tau and efficiently reduces aggregation. This effect is reduced in the aggregation prone conformations, such as those found in P301L tau. Tau is colored according to the repeat domains in red, green, blue and magenta. DnaJC7 is shown in white spheres.